GLOBAL ICE CLOUD OBSERVATIONS: RADIATIVE PROPERTIES AND STATISTICS FROM MODERATE-RESOLUTION IMAGING SPECTRORADIOMETER MEASUREMENTS

A Dissertation

by

KERRY GLYNNE MEYER

Submitted to the Office of Graduate Studies of
Texas A&M University
in partial fulfillment of the requirements for the degree of

DOCTOR OF PHILOSOPHY

August 2007

Major Subject: Atmospheric Sciences

GLOBAL ICE CLOUD OBSERVATIONS: RADIATIVE PROPERTIES AND STATISTICS FROM MODERATE-RESOLUTION IMAGING SPECTRORADIOMETER MEASUREMENTS

A Dissertation

by

KERRY GLYNNE MEYER

Submitted to the Office of Graduate Studies of
Texas A&M University
in partial fulfillment of the requirements for the degree of

DOCTOR OF PHILOSOPHY

Approved by:

Chair of Committee,	Ping Yang
Committee Members,	Gerald North
	Thomas Wilheit
	George Kattawar
Head of Department,	Richard Orville

August 2007

Major Subject: Atmospheric Sciences

ABSTRACT

Global Ice Cloud Observations: Radiative Properties and Statistics from Moderate-resolution Imaging Spectroradiometer Measurements. (August 2007)

Kerry Glynne Meyer, B.S., Texas A&M University;

M.S., Texas A&M University

Chair of Advisory Committee: Dr. Ping Yang

Ice clouds occur quite frequently, yet so much about these clouds is unknown. In recent years, numerous investigations and field campaigns have been focused on the study of ice clouds, all with the ultimate goal of gaining a better understanding of microphysical and optical properties, as well as determining the radiative impact. Perhaps one of the most recognized instruments used for such research is the Moderate-resolution Imaging Spectroradiometer (MODIS), carried aboard the NASA EOS satellites Terra and Aqua. The present research aims to support ongoing efforts in the field of ice cloud research by use of observations obtained from Terra and Aqua MODIS. First, a technique is developed to infer ice cloud optical depth from the MODIS cirrus reflectance parameter. This technique is based on a previous method developed by Meyer et al. (2004). The applicability of the algorithm is demonstrated with retrievals from level-2 and -3 MODIS data. The technique is also evaluated with the operational MODIS cloud retrieval product and a method based on airborne ice cloud observations. From this technique, an archive of daily optical depth retrievals is constructed. Using simple statistics, the global spatial and temporal distributions of ice clouds are determined.

Research has found that Aqua MODIS observes more frequent ice clouds and larger optical depths and ice water paths than does Terra MODIS. Finally, an analysis of the time series of daily optical depth values revealed that ice clouds at high latitudes, which are most likely associated with synoptic scale weather sytems, persist long enough to move with the upper level winds. Tropical ice clouds, however, dissipate more rapidly, and are in all likelihood associated with deep convective cells.

This manuscript is dedicated to all of my family and friends who have aided and supported me throughout my life.

ACKNOWLEDGMENTS

I would like to thank my advisor, Dr. Ping Yang, for his guidance, support, ideas, and patience throughout my work on this project. I greatly appreciate everything he has done for me, and for the opportunity he has given me to continue my education. I would also like to thank my committee member Dr. Gerald North for the direction and assistance he offered during work on the time series analysis. I would like to thank the other members of my advisory committee, Dr. Thomas Wilheit and Dr. George Kattawar, for showing an interest in my research and for the constructive comments they have given me.

I would like to thank Dr. Bo-Cai Gao at the Naval Research Laboratory for his help on my projects and publications. I would also like to thank Drs. Michael King and Steve Platnick for the MODIS visualization software developed by their group.

This study is partly supported by the NASA Earth System Science Fellowship Program (NNG04GQ92H) managed by Dr. Ming-Ying Wei, as well as by the National Science Foundation Physical Meteorological Program managed by Dr. Andrew Detweiler (ATM-0239605) and a NASA research grant (NNG04GL24G) from the Radiation Sciences Program managed by Dr. Hal Maring and NASA MODIS program managed by Dr. Paula Bontempi.

Lastly, I would like to thank my wife Alison, the love of my life, for the loving support and patience she has given me. I would also like to thank my family and friends, especially my parents, my brother, and my grandparents, for all of the support they have given me throughout the years.

TABLE OF CONTENTS

Page

LIST OF FIGURES

FIGURE Page

FIGURE Page

FIGURE Page

1. INTRODUCTION

Visible and sub-visible ice clouds (e.g., cirrus clouds) have a global distribution. Recent observations (Menzel et al., 1983) have shown that cirrus clouds can cover as much as 30% of the entire earth. Thin cirrus clouds are primarily confined to the tropical regions, and their frequency peaks of presence occur sharply over the Western Pacific Ocean, particularly during the boreal winter when the tropopause temperature is at a minimum (Jensen et al., 1996). In fact, a thin cirrus layer may be present as much as 80% of the time in this region (Wang et al., 1994). Because of their large spatial coverage and frequency of occurrence, ice clouds play an important role in the terrestrial atmosphere (Stephens et al., 1990, Liou et al. 1999, Lynch et al., 2002, and references cited there in).

Ice clouds near the tropopause, specifically cirrus clouds, can have a significant radiative impact. Ice clouds reflect shortwave solar radiation back to space (the solar albedo), and trap longwave terrestrial radiation in the atmosphere (the greenhouse effect). Over the tropics, where insolation is largest, ice clouds are observed nearly 70 percent of the time (Meyer et al., 2007). It has been found that, for most cases, net cirrus radiative forcing is positive (i.e., warms the atmosphere), although clouds with a large number of small ice crystals have negative net radiative forcing (Zhang et al., 1999). Such radiative effects can influence global temperature, though the degree to which this

---

This dissertation follows the style and format of Atmospheric Research.

numerically predict the long-term patterns of global temperature, among other parameters, must globally parameterize the microphysics and radiative effects of ice clouds due to their complex nature (i.e., non-spherical particles, etc.). Although recent research has greatly expanded our knowledge of ice clouds, uncertainties still exist in radiative forcing studies, and current GCMs inadequately parameterize the microphysics of such clouds. The need for a better understanding of ice clouds on a global scale, particularly through sophisticated global observations and retrievals, is evident.

At this point, ice clouds are one of the least understood components in the atmosphere due to many uncertainty factors (e.g., cloud height, ice water content, ice crystal size distributions, and particle shapes) that determine the bulk radiative properties of ice clouds (Tsay et al. 1996). As such, a number of field campaigns (e.g., Starr, 1987) have been dedicated to the study of these clouds. In the past two decades, ice clouds have been investigated from various perspectives. The radiative properties of ice clouds have been investigated with surface and airborne measurements (Pilewskie et al., 1998; Baum et al., 2000; Baran et al., 2001; Wendisch et al., 2005). Ice cloud microphysical properties have been derived from radiance measurements obtained by the Geostationary Operational Environmental Satellite (GOES) (Minnis et al., 1993), the Airborne Visible/Infrared Imaging Spectrometer (AVIRIS) (Gao et al., 2004), and the Moderate Resolution Imaging Spectroradiometer (MODIS) (King et al., 2003; Platnick et al., 2003; Meyer et al., 2004). Global statistics of ice clouds have been inferred from the High resolution Infrared Radiation Sounder (HIRS) on the National Oceanic and Atmospheric Administration (NOAA) satellites (Wylie et al., 1994; Wylie and Menzel,

1999; Wylie et al., 2005), and the distribution of thin cirrus clouds has been determined from the MODIS on the Terra spacecraft (Dessler and Yang, 2003).

The retrieval of cloud microphysical and optical properties from space-borne measurements has been a major effort of the remote sensing community. In particular, the MODIS on board both the Terra and Aqua satellites have been especially productive tools for ice cloud analysis, and its dataset is used extensively in the present research. Terra and Aqua were launched into orbit as part of the NASA (National Aeronautics and Space Administration) Earth Observing System (EOS), with Terra MODIS (morning orbit, descending across the equator at 10:30 local time) beginning observations in February, 2000, and Aqua MODIS (afternoon orbit, ascending across the equator at 2:30 local time) beginning observations in August, 2002. The MODIS passively views the earth's atmosphere, land, and oceans in 36 spectral bands ranging from the visible to the infrared. Of these bands, the 1.375 μm channel, located in a strong water vapor absorption band, is quite effective for detecting ice clouds (Gao and Kaufman, 1995).

The research presented here is intended to contribute to the current knowledge of ice cloud microphysical properties and to the development of a "climatology" of global ice clouds using various statistical tools. A general methodology, coupled with a brief discussion of several key science concepts fundamental to the current research, is detailed in Section 2. In Section 3, a technique to infer global ice cloud optical depth is introduced. This technique is derived from a previous method to retrieve tropical cirrus cloud optical depth (Meyer et al., 2004). A detailed analysis of global ice clouds, using simple statistics, is detailed in Section 4. Section 5 discusses a time series analysis of

daily ice cloud optical depth using correlation calculations. Finally, the summary and conclusions are discussed in Section 6.

2. METHODOLOGY

2.1 Objectives

The objectives of the research presented here are to:

- Develop a global ice cloud optical depth retrieval technique with basic assumptions consistent with those of the operational MODIS cloud retrieval algorithms.
- Determine the spatial and temporal patterns of ice clouds (i.e., develop an ice cloud "climatology") from a global perspective using MODIS observations from both the Terra and Aqua satellites.
- Determine the nature of ice clouds in the Earth's atmosphere (source/sink regions, general movements, etc.) by means of a time series analysis of daily mean ice cloud optical depth values derived from the aforementioned global retrieval.

A brief synopsis of several key concepts and methods, forming the foundation for the research presented here, follows.

2.2 DISORT

An essential component of remote sensing applications is the radiative transfer model. Here, all radiative transfer calculations are computed using the Discrete Ordinates Radiative Transfer (DISORT) algorithm (Stamnes et al., 1988), a method based on the well-known radiative transfer theory of Chandrasekhar (1950). The

DISORT algorithm models the scattering and emittance of monochromatic radiation (including all wavelengths in the spectrum from ultraviolet to microwave) in a discrete-layered medium.

Each layer in the relevant medium is user-defined, such that the optical properties, chemical composition, temperature, and so forth, must be specified. For application to the Earth's atmosphere, clouds of different types (such as water, ice, or mixed phase) may be inserted into the medium as layers in a number of ways: as a single layer, as multiple layers, etc. Subsequently, DISORT requires as input the bulk-scattering properties, as well as the pre-defined cloud optical depth, of each user-defined cloud layer. For ice clouds, such bulk-scattering parameters include the ice crystal mean effective diameter, the extinction coefficient, the single-scattering albedo, the asymmetry parameter, the percentage of delta-transmission, the truncation energy, and the scattering phase function.

Because the scattering phase function is highly non-linear, it is normally expanded, for computational purposes, in terms of Legendre polynomials. For ice clouds, the size of the ice crystals composing such clouds is much larger than the incident wavelength of solar radiation, the consequence of which is a phase function strongly peaked in the forward direction (i.e., large forward scattering). Such forward peaks typically require thousands of Legendre polynomials for phase function expansion. However, truncation of this forward peak greatly reduces the number of polynomials needed for expansion. Previously, this had been accomplished using the delta-M method (Wiscombe, 1977); here, the δ-fit method of Hu et al. (2000) is used. The δ-fit method, an extension of

delta-M, calculates the coefficients of the Legendre polynomial expansion using least-squares fitting designed to minimize the difference between the approximate phase function and the actual phase function. This gives an improved phase function estimation at large scattering angles than the previous delta-M method (Hu et al., 2000).

2.3 Cirrus Reflectance

The ability to study ice clouds was greatly enhanced with the decision to include the 1.375 μm wavelength channel (Gao and Kaufman, 1995) in the MODIS spectral bands. This channel is unique in that ice crystals are highly reflective at this wavelength, while water droplets are not. It is also located in a strong water vapor absorption region, which significantly reduces the likelihood that surface reflection within this channel escapes to space (since most of the radiation in this channel is absorbed by atmospheric water vapor). The consequence of these unique characteristics is that the 1.375 μm radiance measured by MODIS is due essentially to ice cloud reflection. The 1.375 μm channel therefore offers an extraordinary opportunity for ice cloud research.

Several techniques based on the 1.375 μm wavelength channel have been developed for ice cloud retrievals. Of primary interest to the present research is an algorithm (Gao et al., 2002) developed to infer isolated visible cirrus (i.e., ice cloud) reflectance using a combination of the 1.375 μm channel and a visible channel (wavelengths ranging from 0.4 to 0.7 μm). This technique divides the atmosphere into three layers: the top layer, composed of the water vapor above ice clouds; the middle layer, composed of the ice clouds; and the bottom layer, composed of the surface, low-level water clouds, aerosols,

and water vapor. The top layer acts to attenuate the 1.375 μm radiation, while the bottom layer absorbs the remaining radiation. Combining the 1.375 μm channel with a visible channel allows for the removal of the effects of the bottom layer on reflectance in the visible channel, resulting in reflectance due solely to ice clouds. This "cirrus reflectance" is currently a parameter in the operational MODIS cloud products. An example of the power of this technique is shown in Fig. 1. Fig. 1(a) is a false color RGB image (0.66, 0.55, and 0.47 μm) of a scene over the Caribbean obtained from Aqua MODIS on April 1, 2007. Fig. 1(b) shows the 1.375 μm reflectance corresponding to (a). Note the absence of surface features and low-level water clouds. Fig. 1(c) is the isolated visible cirrus reflectance derived from the 1.375 and 0.66 μm channels. This image is scaled as indicated by the color bar at right. Note that all surface features and low-level water cloud contamination have been removed.

2.4 Tropical Cirrus Optical Depth

Previously, a method was introduced (Meyer et al., 2004) to infer tropical cirrus cloud optical depth from the MODIS visible cirrus reflectance parameter. The retrieval follows a simple look-up table approach, with cirrus reflectance converted to cloud optical depth on a pixel specific basis (i.e., a different look-up table is used for each MODIS pixel).

Retrieval look-up tables, consisting of 23 discrete optical depths paired with the corresponding visible cirrus reflectance values, are generated with the DISORT method. To simulate the MODIS cirrus reflectance (computed here in the 0.66 μm channel),

DISORT is run with a single-layer cirrus cloud in a transparent atmosphere (i.e., no absorption/reflection resulting from atmospheric gases/aerosols) with no surface reflection. Theoretically calculated bulk-scattering properties of cirrus clouds, used as input for DISORT, are computed by averaging the single-scattering properties of Yang et al. (2000) over a prescribed ice particle habit (i.e., shape) distribution and nine tropical cirrus cloud particle size distributions derived from in-situ observations obtained during the Central Equatorial Pacific Experiment (CEPEX). The ice particle habit distribution, a universal ice crystal shape "recipe" for cirrus clouds, is comprised of 33.7% solid columns, 24.7% bullet rosettes, and 41.6% aggregates (McFarquhar, 2000).

Sample look-up tables for four distinct view geometries (solar/satellite zenith angles and relative azimuth angle) are shown in Fig. 2. Each table contains nine plots representing different ice crystal effective diameters (D_{eff}), one for each CEPEX size distribution. Because there appears to be little dependence on effective size, the plot corresponding to the median effective size ($D_{eff} = 34.97$ μm) was selected as the look-up table. A look-up library was then generated, consisting of 4864 view geometry dependent look-up tables (solar/satellite zenith angles from 0 to 75 degrees, relative azimuth angles from 0 to 180 degrees) with 23 optical depth/cirrus reflectance pairs (optical depths from 0.002 to 100.0).

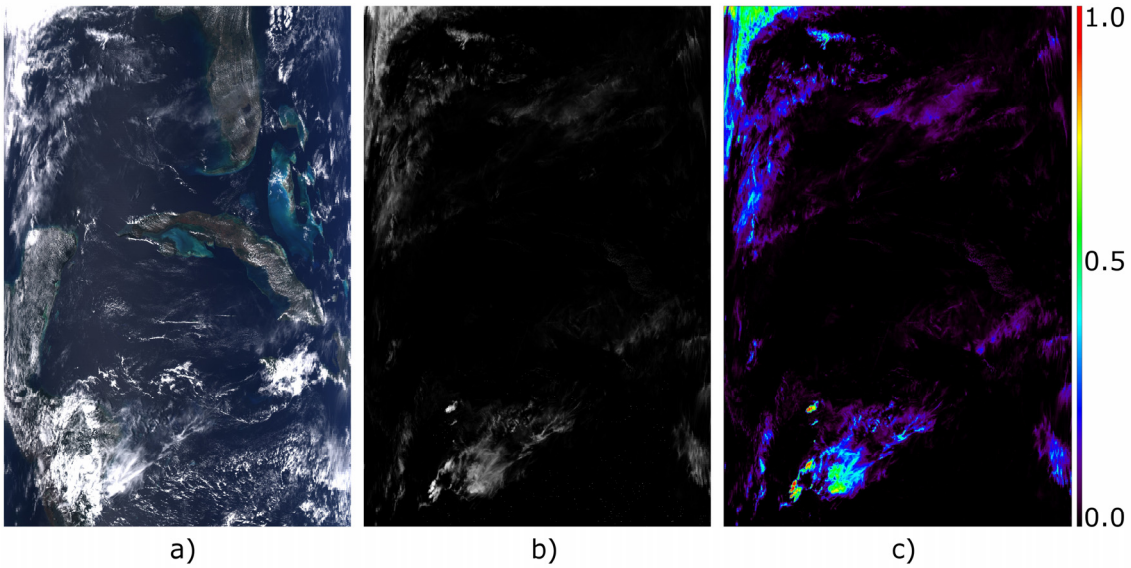

Fig. 1. Sample MODIS granule from Aqua on April 1, 2007. (a) False color RGB image (0.66, 0.55, and 0.47 μm). (b) Observed 1.375 μm reflectance corresponding to (a). (c) Derived isolated visible cirrus reflectance.

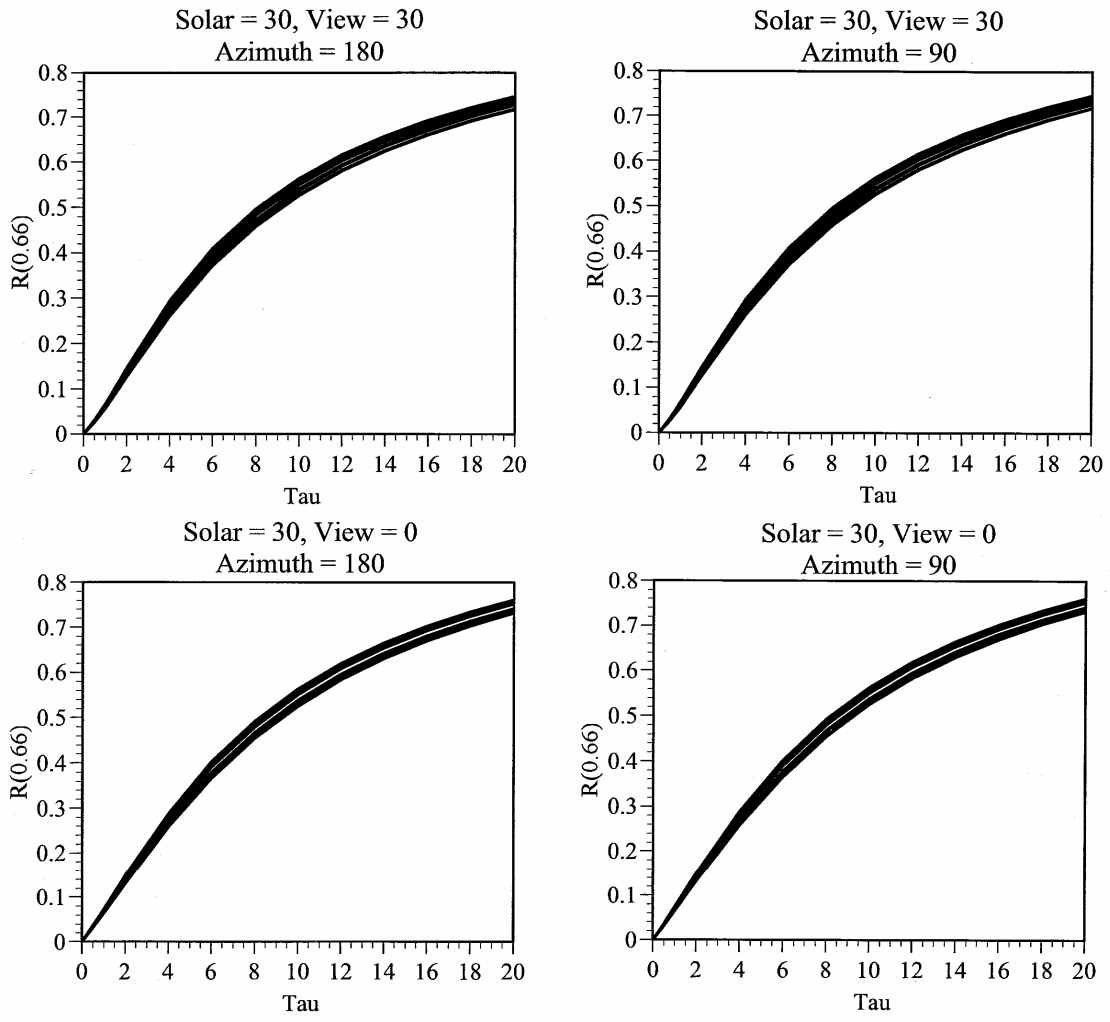

Fig. 2. Sample look-up tables for tropical cirrus cloud optical depth retrieval.

Fig. 3 shows a sample retrieval for a granule of Terra MODIS data taken on July 11, 2002, over the Caribbean Sea. Fig. 3(a) is a false color RGB image using reflectance measurements in three visible channels (0.66, 0.55, and 0.47 μm). Fig. 3(b) shows the corresponding 1.375 μm reflectance. Note that, unlike the visible image in (a), surface features and low-level water clouds are not visible in this image. Fig. 3(c) shows the retrieved cirrus cloud optical depth. This image is scaled as shown by the color bar at right. The algorithm's capability to retrieve small optical depths (regions shaded in violet), which indicate thin cirrus, is quite evident here.

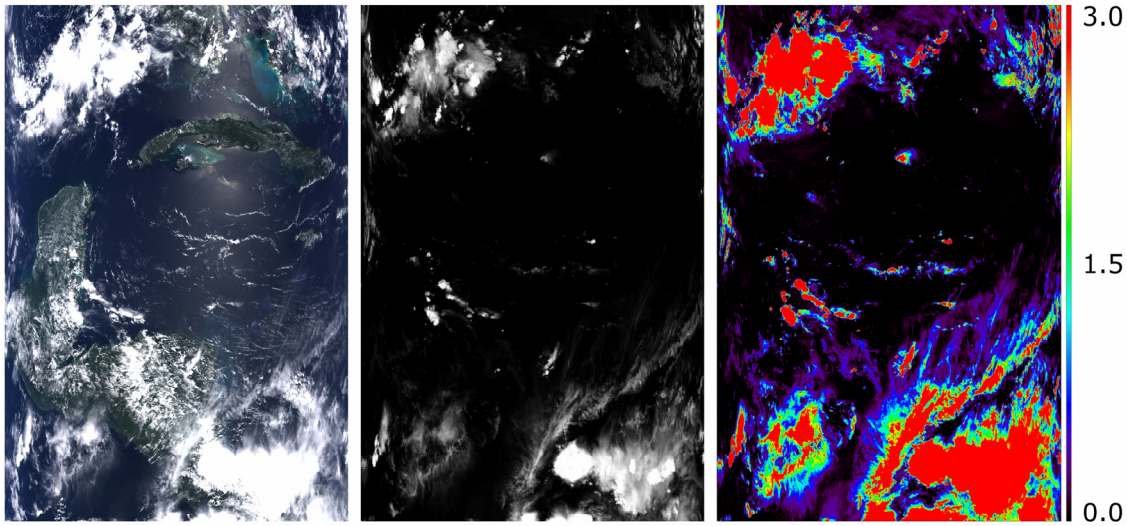

Fig. 3. Sample tropical cirrus cloud optical depth retrieval. (a) False color RGB image (0.66, 0.55, and 0.47 μm) from Terra MODIS over the Caribbean Sea on July 11, 2002. (b) 1.375 μm reflectance corresponding to (a). (c) Retrieved cirrus cloud optical depth corresponding to (a) and (b).

3. ICE CLOUD OPTICAL DEPTH FROM GLOBAL MODIS OBSERVATIONS

3.1 Method

The present method, a modification of the technique (Meyer et al., 2004) detailed in Section 2.4, follows a straightforward algorithm to retrieve ice cloud optical depth. Visible cirrus reflectance data, taken from the MODIS atmosphere product, are converted to ice cloud optical depth by use of pre-calculated look-up tables. A library of such look-up tables is constructed from radiative transfer calculations using the DISORT method (Stamnes et al., 1988). The applicability of this technique is illustrated using several examples from Aqua MODIS. The technique is also evaluated with similar results from the operational MODIS cloud retrieval algorithms (King et al., 1997; Platnick et al., 2003), as well as with in-situ aircraft measurements coinciding with MODIS overpasses.

3.1.1 Bulk Scattering Properties

Constructing the look-up library necessary for ice cloud optical depth retrieval

requires realistic bulk scattering properties of ice clouds for the radiative transfer calculations. To remain consistent with the operational MODIS atmosphere product, the bulk scattering properties (Baum et al., 2005 I,II) developed for the MODIS Collection 5 cloud retrieval algorithms are used here, representing the primary difference between the current method and that of Meyer et al. (2004) (hereafter referred to as the Collection 004 retrieval). These scattering properties were developed assuming a habit distribution, or mixture of idealized ice crystal shapes, consisting of bullet rosettes, solid and hollow columns, plates, aggregates, and droxtals. Specifically, ice crystals with maximum dimension less than 60 μm are assumed to be 100% droxtals; crystals with maximum dimension between 60 and 1000 μm are assumed to be 15% bullet rosettes, 50% solid columns, and 35% plates; crystals with maximum dimension between 1000 and 2500 μm are assumed to be 45% hollow columns, 45% solid columns, and 10% aggregates; crystals with maximum dimension between 2500 and 9500 μm are assumed to be 97% bullet rosettes and 3% aggregates.

The bulk scattering properties are computed by averaging the single-scattering properties of the individual ice crystal habits over the prescribed habit distribution and ice particle size distributions obtained from in-situ observations. Included are parameters such as the mean effective diameter, extinction efficiency, single-scattering albedo, asymmetry factor, and fraction of delta-transmission, as well as the normalized phase function computed at 498 scattering angles (from 0 to 180˚). The bulk scattering properties used here are computed for 18 effective diameters, ranging from 10 to 180 μm (Baum et al., 2005 I,II).

Fig. 4 shows the normalized scattering phase functions of all 18 effective diameters for the band centered at 0.66-μm. Red lines indicate effective diameters less than or equal to 60 μm. Note the presence of the 22˚ and 46˚ halos (peaks in the phase function), phenomena resulting from the hexagonal shapes of the ice particles. These halos diminish as the effective size decreases. The strong forward peaks exhibited here result from the relatively large size of the ice crystals compared to the wavelengths. For the DISORT calculations used to compute the look-up library, the forward peaks are truncated and the phase functions are expanded in terms of Legendre polynomials using the δ-fit method (Hu et al., 2000) with 32 streams. These bulk-scattering properties offer a significant improvement over previous versions (Baum et al., 2005 I,II).

3.1.2 Look-up Library

The retrieval look-up library consists of 4864 pre-calculated look-up tables, each categorized by the geometrical configuration of the sun and the satellite (i.e., the solar/satellite zenith angles and relative azimuth). Each look-up table consists of visible ice cloud reflectance values calculated for 23 optical depths ranging from 0.002 to 100.0. To effectively simulate visible cirrus reflectance, the look-up tables, constructed from DISORT calculations, are generated under the assumption of a single-layer ice cloud in a transparent atmosphere with no surface reflectance; i.e., the reflection and scattering in this system are due only to the ice cloud layer.

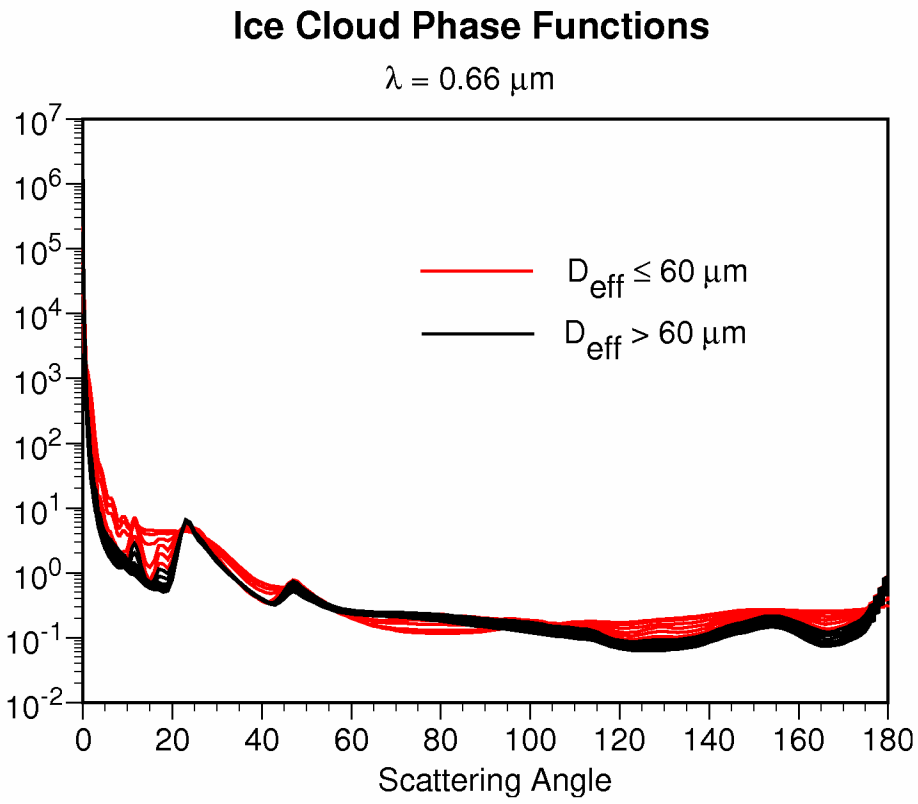

Fig. 4. Normalized scattering phase functions for the 18 effective diameters (from 10 to 180 μm) used in this study.

Under the above habit distribution, preliminary DISORT calculations reveal that, unlike under the Collection 004 retrieval assumptions, cirrus reflectance values are sensitive to ice particle effective size. This sensitivity results in a shift in the look-up table when moving from one effective size to the next. To account for this, an effective particle size is assumed for all ice clouds. Previously, it was found that the peak in the global distribution of ice cloud particle effective diameter (D_{eff}), obtained from the operational MODIS Collection 004 dataset, is around 50 μm (Hong et al., to be published). Fig. 5, a histogram of mean effective diameters obtained from four years of the Aqua MODIS level-3 Collection 5 atmosphere product, reveals similar results. For the present study, the scattering properties associated with an effective diameter of 50 μm are used to compute the look-up tables.

Fig. 6 shows a sample look-up table (the solid curve) generated for an effective particle diameter of 50 μm. The solar and satellite zenith angles are 30˚ and 0˚, respectively, and the relative azimuth angle is 60˚. Uncertainty estimates, in terms of the standard deviation of ice particle effective size (σ_{deff} = 17.0μm, calculated from the data in Fig. 5), are shown as horizontal lines. The solid horizontal lines correspond to uncertainties due to errors in effective diameter of $\pm\sigma_{deff}$, the dotted lines to errors of $\pm 2\sigma_{deff}$. When cirrus reflectance is small, the absolute uncertainties in optical depth are significantly less than when reflectance is large. Relative uncertainties corresponding to $\pm\sigma_{deff}$ errors range from roughly -14% to 9%.

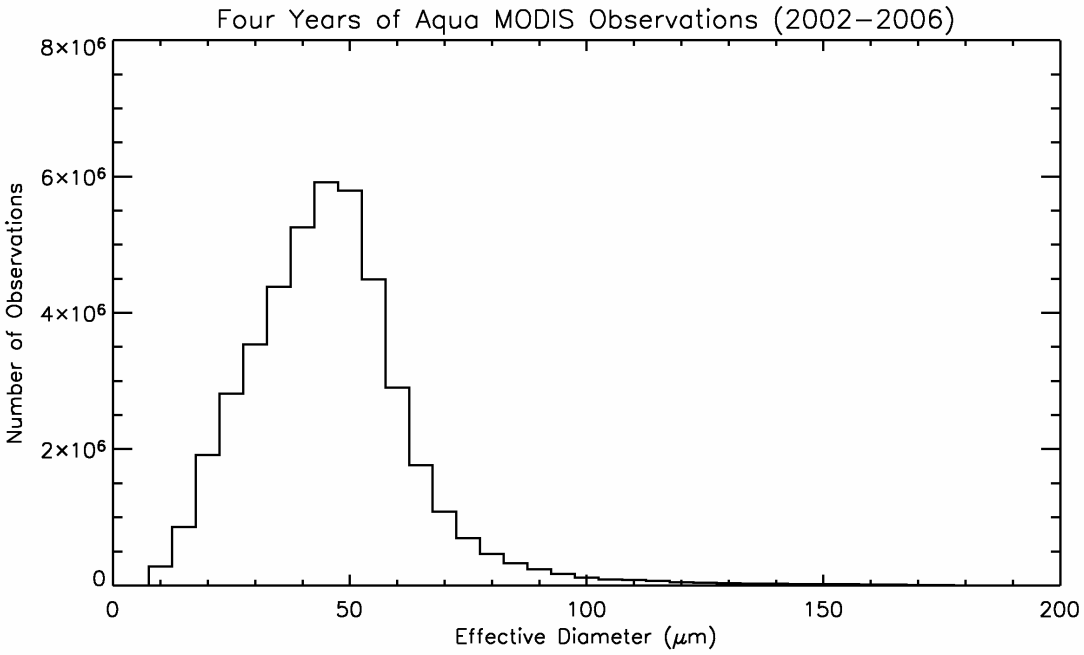

Fig. 5. Histogram of retrieved mean ice particle effective diameter from four years of Aqua MODIS observations (September, 2002 through August, 2006). Effective diameter data are taken from the operational MODIS Collection 005 atmosphere product.

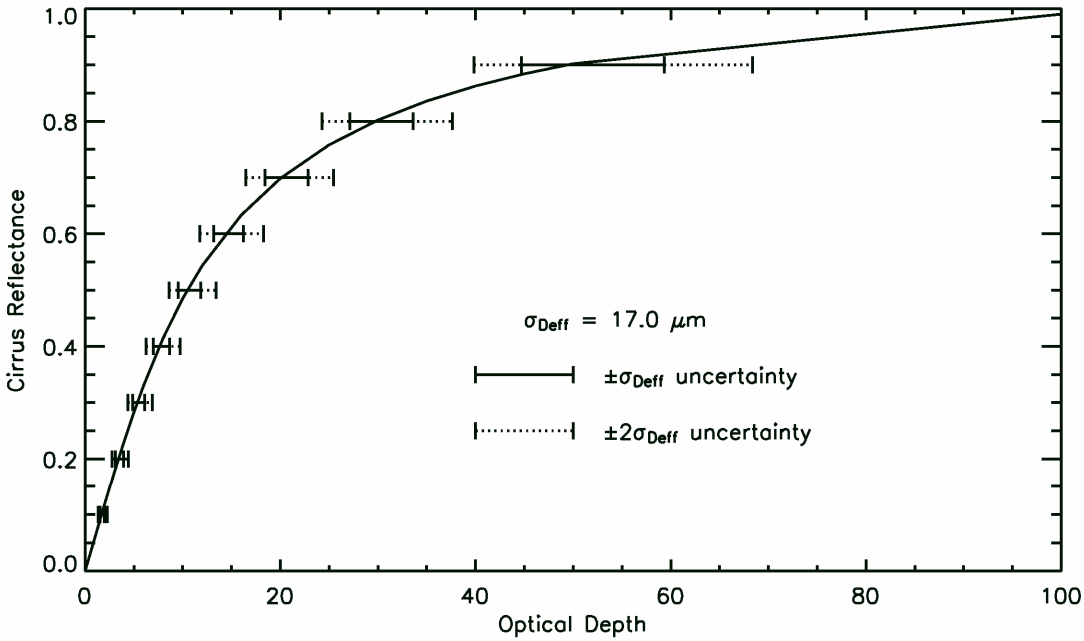

Fig. 6. Sample look-up table for solar and satellite zenith angles of 30˚ and 0˚, respectively, and a relative azimuth angle of 60˚, assuming an ice particle effective diameter of 50 μm. Solid (dotted) horizontal lines denote optical depth uncertainties due to ±1 standard deviation (±2 standard deviation) errors in effective diameter.

A comparison between look-up tables for the present method and the Collection 004 retrieval is shown in Fig. 7. Here, look-up tables corresponding to each retrieval are plotted for eight different view geometries, consisting of two solar and satellite zenith angles (denoted SZen and VZen, respectively) and two relative azimuth angles (denoted RAzim). Solid lines denote the Collection 004 retrieval, dotted lines denote the current method. Mean relative errors are shown in each plot. Note that the absolute errors between the two methods are relatively small. However, mean relative errors (calculated with respect to the present method) range from approximately 15% to 24%, as the Collection 004 retrieval consistently underestimates ice cloud optical depth.

3.2 Results

The applicability of the present method is demonstrated using cirrus reflectance data from the MODIS on Aqua. Both level-2 (1 km resolution) and level-3, or global, retrievals are shown here. The level-3 dataset has a 1 degree spatial resolution, and consists of parameters statistically derived from the level-2 retrievals. In addition, the retrieval is evaluated using the operational MODIS cloud retrieval algorithm and in-situ aircraft measurements.

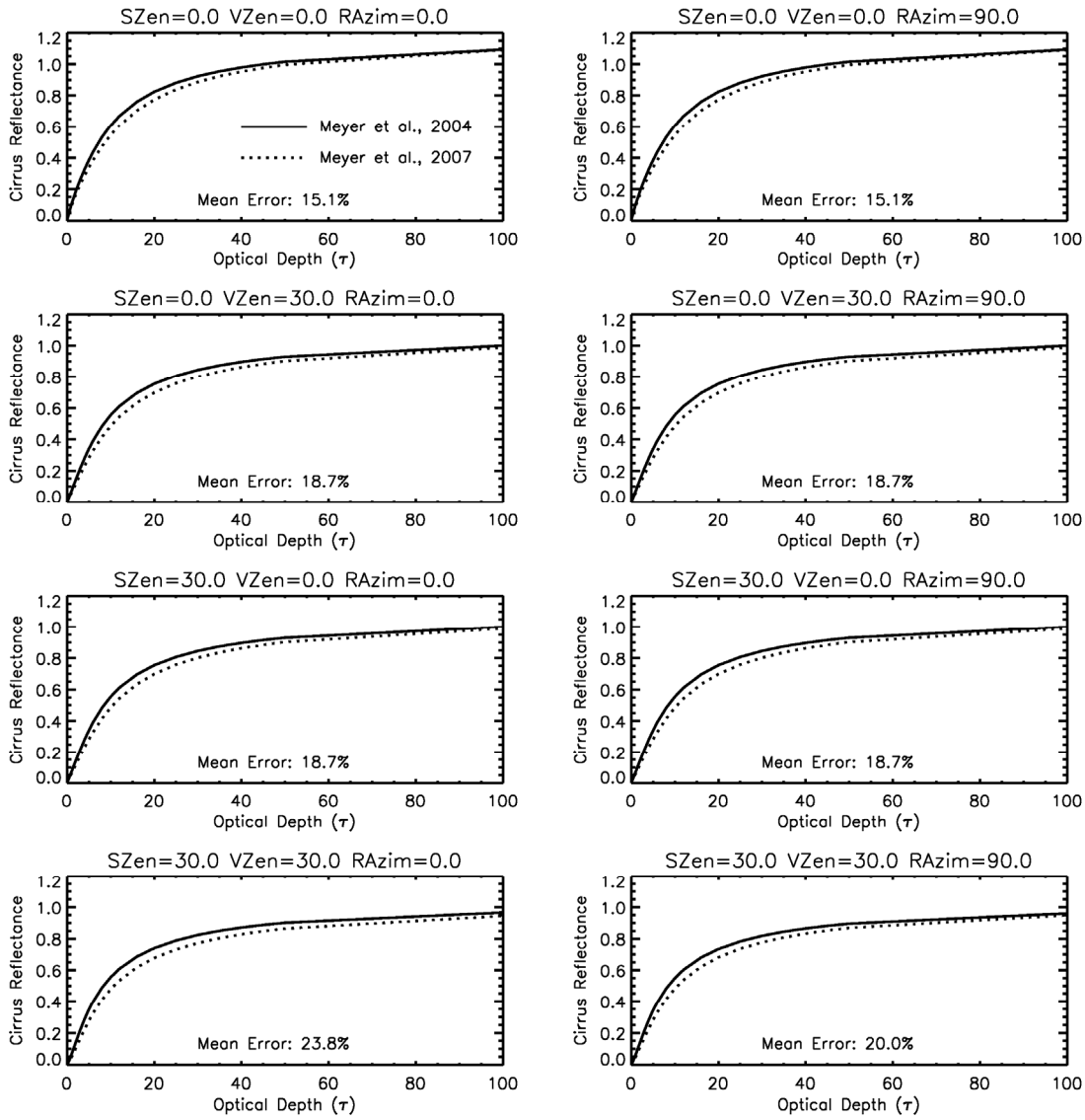

Fig. 7. Comparison between the look-up tables of the present ice cloud optical depth retrieval method (Meyer et al., 2007) and those of the previous method (Meyer et al., 2004). Mean errors, shown at the bottom of each plot, are with respect to the present method.

The retrieval itself is straightforward. Because measured cirrus reflectance is dependent on scattering angle, the sun/satellite view geometry is used to select the appropriate look-up table for each data point. The visible cirrus reflectance is then matched with the corresponding ice cloud optical depth along the curve in the look-up table. For example, using the look-up table shown in Fig. 6, a cirrus reflectance of 0.25 roughly corresponds to an ice cloud optical depth around 5. Minimum cirrus reflectance considered here is 0.005; pixels with cirrus reflectance below this threshold are considered to be clear sky.

Fig. 8 shows a sample level-2 retrieval using cirrus reflectance data derived from Aqua MODIS observations over the southern Pacific Ocean on March 1, 2007. Fig. 8(a) is a false color RGB image generated from level-1b 0.66, 0.55, and 0.47 μm reflectance. Fig. 8(b) is the 1.375 μm reflectance corresponding to (a). Fig. 8(c) shows the ice cloud optical depth, retrieved from the level-2 cirrus reflectance parameter, corresponding to (a) and (b). This image is scaled as indicated by the color bar at right. Note the sensitivity to thin cirrus clouds, denoted by the regions of violet.

Fig. 9 shows ice cloud optical depth, retrieved using the current Collection 005 method (a) and the previous Collection 004 method (b), corresponding to the MODIS granule in Fig. 8. Both images are scaled as indicated by the color bars. Note the similarities between each image. However, as illustrated by Fig. 7, the Collection 004 retrieval underestimates optical depth with respect to the current method. This is clearly visible throughout the thicker regions of the cloud.

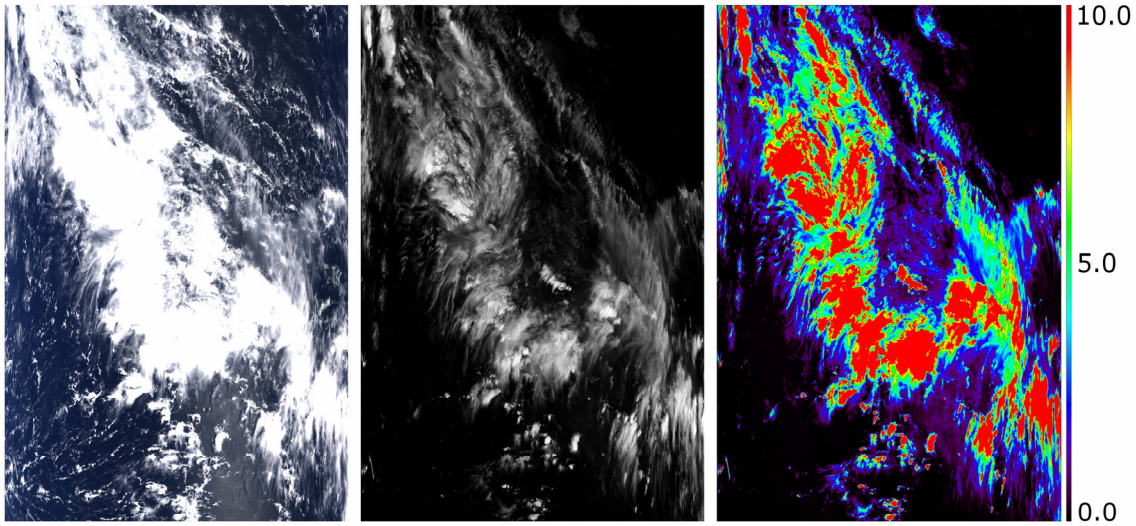

Fig. 8. Sample level-2 retrieval using cirrus reflectance data derived from Aqua MODIS observations over the southern Pacific Ocean on March 1, 2007. (a) False color RGB image (0.66, 0.55, and 0.47 μm). (b) 1.375 μm reflectance corresponding to (a). (c) Retrieved cirrus cloud optical depth corresponding to (a) and (b).

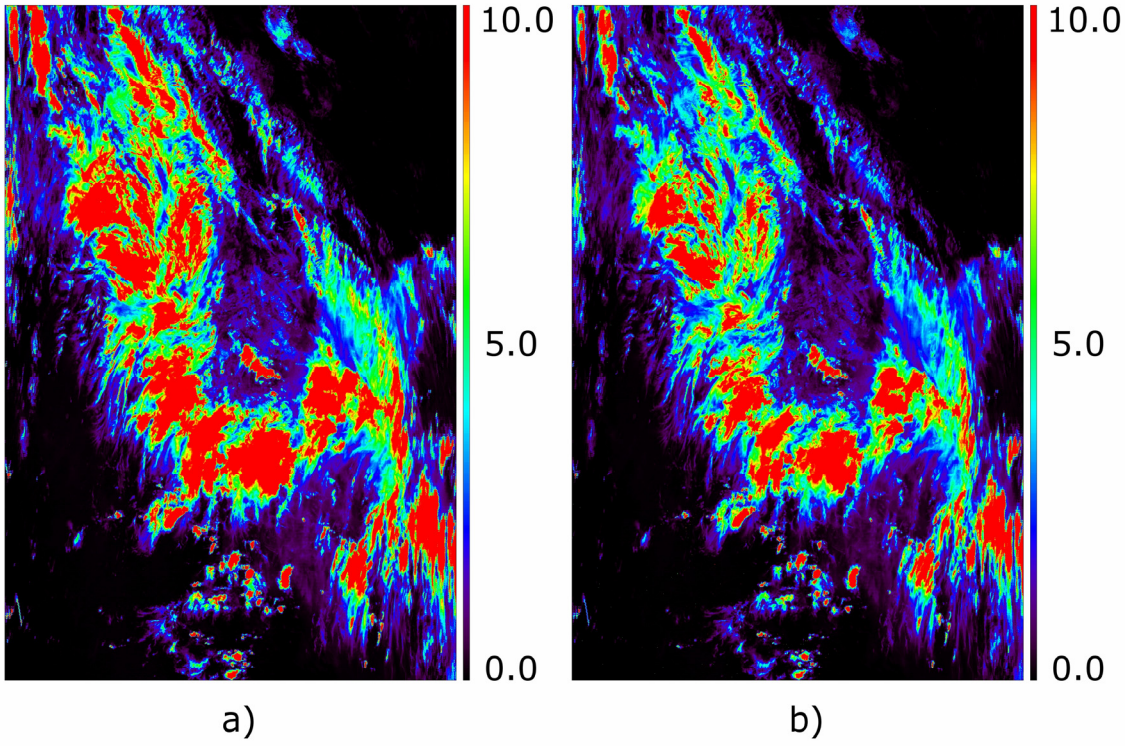

Fig. 9. Ice cloud optical depth, corresponding to the granule in Figure 4, retrieved from (a) the current Collection 005 retrieval and (b) the previous Collection 004 retrieval.

Fig. 10 shows a scatter plot of the ice cloud optical depth values from both retrievals shown in Fig. 9. The banding features in the plot result from viewing angle effects. This plot further illustrates the underestimation of optical depth by the Collection 004 retrieval.

Fig. 11(a) shows the global derived MODIS cirrus reflectance observed by Aqua on April 23, 2006. The image is scaled as shown by the color bar. Black regions denote missing data, while violet regions have cirrus reflectance at or near zero. Red regions correspond to cirrus reflectance values of 0.2 or greater. Note the absence of data in the southern polar region, due to the daytime only aspect of this retrieval. Also, orbital tracks are clearly evident in the tropics.

Fig. 11(b) shows the retrieved ice cloud optical depth corresponding to the reflectance data in Fig. 11(a). Similar to Fig. 11(a), black regions denote missing data, violet regions denote optical depths at or near zero, and red regions denote optical depths of 5 or greater. In this image, the tropical region appears to have less missing data than in that of Fig. 11(a). This is because data points with cirrus reflectance equal to zero are reported as missing data in the operational dataset. Here, sensor pixel counts are used to identify such data points, which are then set to zero.

Fig. 11(c) shows the operationally retrieved MODIS ice cloud optical depth for April 23, 2006. Note that, especially over the tropics, the observable patterns in Fig. 11(b) and (c) are similar. Note also that this image has larger values of optical depth than those in Fig. 11(b). This is because the MODIS operational retrieval is a total column optical

depth, whereas the present method is limited exclusively to the contribution by ice clouds.

Fig. 12(a) shows the Aqua MODIS derived global cirrus reflectance for October 23, 2006. This image is scaled similar to that in Fig. 11(a). Note here, in contrast to Fig. 11(a), the missing data over the northern polar region, due to the seasonal solar patterns. Orbital tracks are clearly evident, as well.

Fig. 12(b) shows the retrieved ice cloud optical depth corresponding to the reflectance data in Fig. 12(a). This image is scaled similar to that in Fig. 12(a). As in Fig. 11(b), there is less missing data over the tropics than is illustrated by the cirrus reflectance image.

Fig. 12(c) shows the MODIS operational ice cloud optical depth for October 23, 2006. Much like the images in Fig. 11, this image has larger values of optical depth than those shown in Fig. 12(b). Again, the location and patterns of ice clouds, especially across the tropics, compare well between Fig. 12(b) and (c).

3.2.1 Retrieval Evaluation

The current method is evaluated using similar results from the MODIS operational ice cloud optical depth retrieval, as well as from in-situ aircraft measurements obtained during various field campaigns.

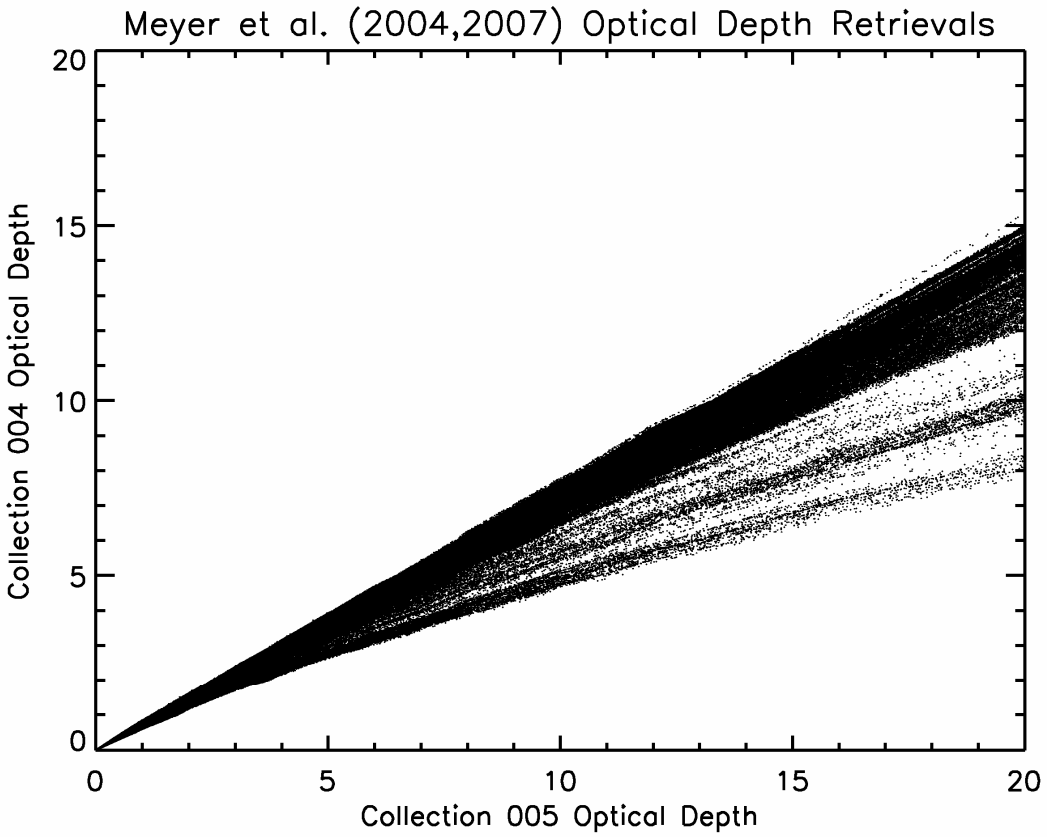

Fig. 10. Scatter plot of the ice cloud optical depth values shown in Fig. 9.

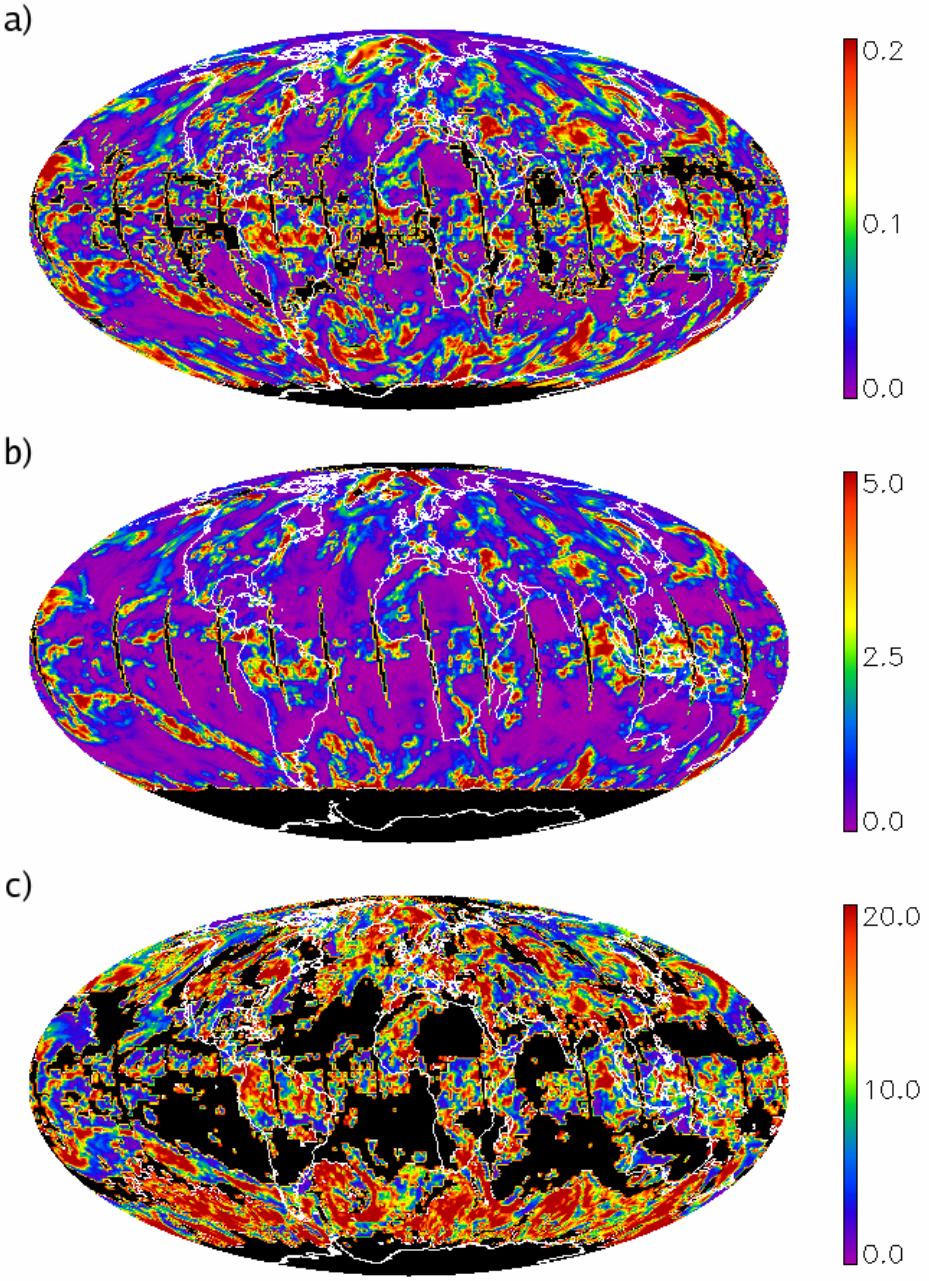

Fig. 11. Sample level-3 retrieval from Aqua MODIS on April 23, 2006. (a) Derived cirrus reflectance. Regions of black denote missing data. (b) Retrieved optical depth corresponding to the cirrus reflectance image shown in (a). (c) MODIS operational ice cloud optical depth for the same day.

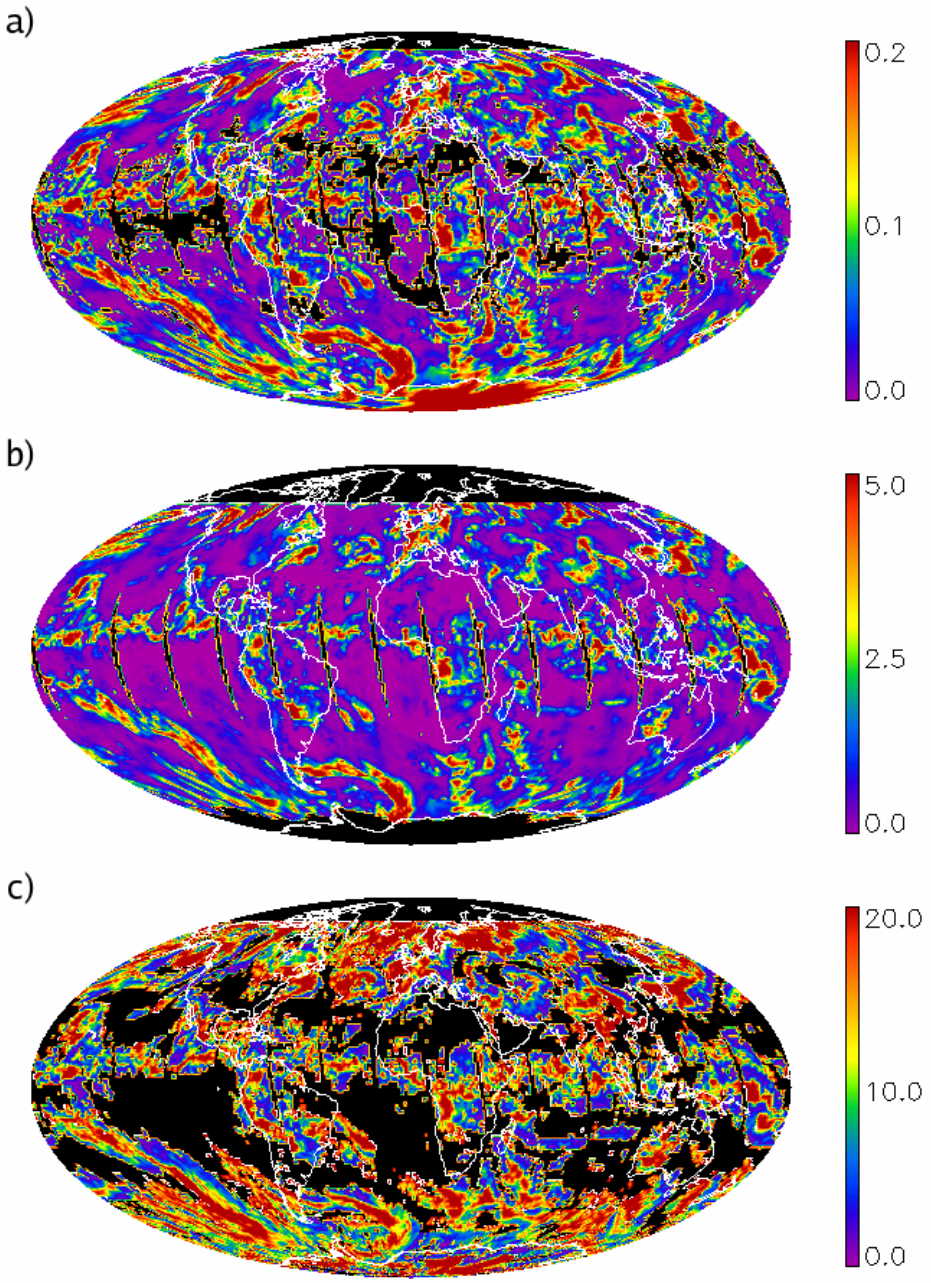

Fig. 12. Sample level-3 retrieval from Aqua MODIS on October 23, 2006. (a) Derived cirrus reflectance. Regions of black denote missing data. (b) Retrieved optical depth corresponding to the cirrus reflectance image shown in (a). (c) MODIS operational ice cloud optical depth for the same day.

Comparing to the operational MODIS cloud retrieval algorithm is quite complicated. The operational algorithm is a bi-spectral technique developed to simultaneously retrieve cloud optical depth and particle effective size (King et al., 1997; Platnick et al., 2003) for both ice and water clouds. A complex cloud phase decision tree is used to determine if a given cloudy pixel is water, ice, mixed phase, or multi-layered, from which follows a phase dependent retrieval using a look-up table approach. Look-up tables are constructed using combinations of a water absorbing channel (1.6, 2.1, and 3.7 μm), sensitive to particle effective size, and a non-absorbing channel (0.66, 0.86, and 1.2 μm), sensitive to optical depth. The choice of the non-absorbing channel is dictated by underlying surface type (e.g., the 0.66, 0.86, and 1.2 μm channels are used for land, ocean, and ice/snow, respectively), such that surface reflection is minimized. For absorbing channels, the reported optical depth is retrieved using the 2.1 μm channel (retrievals using the 1.6 and 3.7 μm channels are similar to those using the 2.1 μm channel because sensitivity to optical depth lies in the non-absorbing bands).

Complications result from several different aspects of this retrieval. Very thin cirrus clouds, which are detectable in the 1.375 μm channel and, thus, the cirrus reflectance parameter, are often missed by the cloud phase decision tree (such pixels may be flagged as clear sky or, in the case of an underlying water cloud, as water). In addition, optical depth retrieved from the operational algorithm can be considered a total column optical depth; that is to say, all clouds within a given column of atmosphere contribute to the optical depth reported by the operational retrieval. In cases of multi-layer clouds,

specifically those involving ice clouds overlapping water clouds, this can lead to a significant overestimation of ice cloud optical depth.

These effects are quite evident when looking at the operational MODIS retrieval corresponding to the granule in Fig. 8 and 9. Fig. 13 shows the operationally retrieved ice cloud optical depth corresponding to this granule. The scaling of the image is identical to those in Fig. 9. Note the preponderance of optical depths greater than 10 throughout the middle portions of the image. Comparing this image to Fig. 9, the operational retrieval reports optical depths much greater than those of both the current and previous techniques, although around cloud edges, a cursory glance reveals these methods may be in reasonable agreement. Note also that, at least in this granule, the MODIS cloud phase decision tree performs quite well, identifying ice clouds in the same regions as those shown in Fig. 9.

A scatter plot comparing the operational retrieval to the current retrieval is shown in Fig. 14. It is broken down into four categories: black, red, and green denote pixels in which the MODIS cloud phase decision tree determines ice, not ice, and multilayer ice clouds, and the blue denotes pixels in which the current retrieval was run but the operational retrieval was not. The overestimation of the operational retrieval is quite evident in this plot. In pixels determined to be clouds other than ice, the operational retrieval misses some thin cirrus clouds with optical depths upwards of four. As was expected, the operational retrieval overestimates the optical depth of multilayer ice clouds (i.e., ice clouds over water clouds). It also significantly overestimates optical depth in pixels deemed ice cloud. These pixels are mostly across the center of the

image, in what appears to be deep convective clouds with ice cloud tops. Nonetheless, there is a dense band clustered around the one-to-one line at small optical depths (less than five) that suggests agreement between the two methods. These pixels are most likely located near cloud edge, where ice clouds do not overlap lower water clouds.

Finally, the current technique is evaluated using in-situ aircraft measurements taken from the Midlatitude Cirrus Cloud Experiment (MidCiX). Researchers at the University of Colorado operate a closed-path tunable diode laser hygrometer (CLH), which measures water vapor from evaporated cloud particles collected through a heated inlet (Hallar et al., 2004). Davis et al. (2007) showed that ice cloud optical depth can be derived from ice water content (IWC) calculated from the CLH observations and measurements of the extinction coefficient. During MidCiX, the CLH was flown aboard the NASA WB57F aircraft from mid April 2004 through late May 2004.

The WB57F flew upward and downward spirals through several cases of cirrus clouds coincident with Terra and Aqua MODIS overpass, providing an excellent opportunity for evaluation of the current retrieval. Here, two cases are selected for the evaluation. Fig. 15(a) and (b) show false color RGB images (0.66, 0.55, and 0.47 μm) obtained from Aqua MODIS on May 2, 2004, and May 3, 2004, respectively. Red boxes denote the approximate regions containing WB57F spirals.

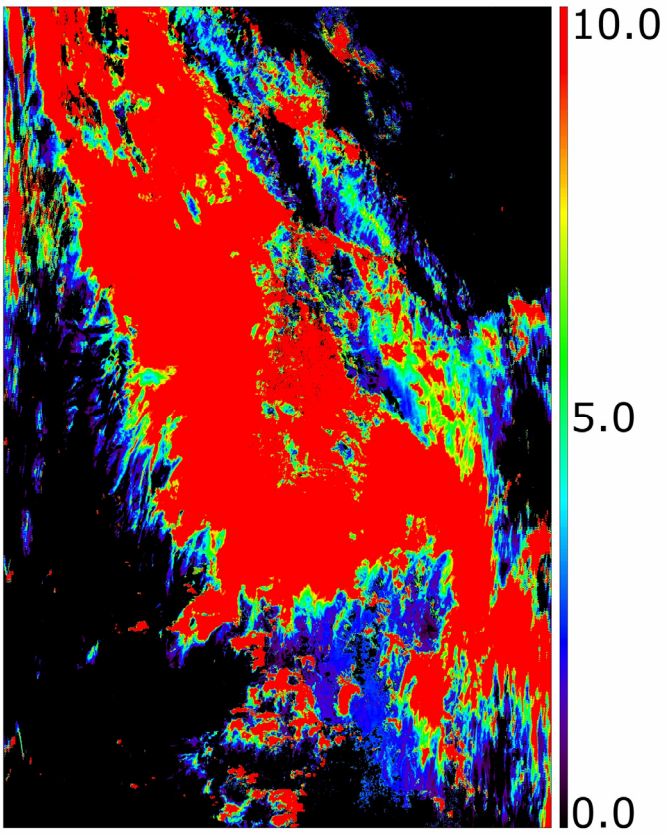

Fig. 13. Ice cloud optical depth, corresponding to the images in Figure 7, obtained from the operational MODIS cloud retrieval algorithm.

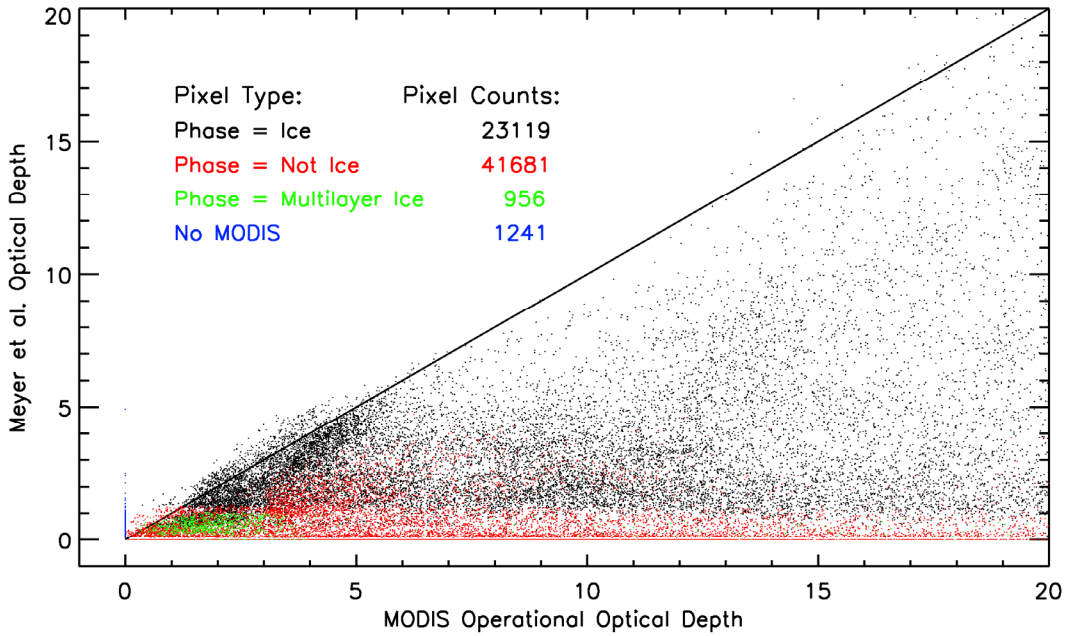

Fig. 14. Scatter plot of Meyer et al. (2007) optical depth retrieval vs. the operational MODIS cloud product optical depth corresponding to the granule in Fig. 8 and 9. Black, red, and green dots denote pixels in which the MODIS cloud phase detection tree determined ice clouds, not ice clouds, and multilayer ice clouds, respectively. Blue dots denote pixels in which the MODIS algorithm was not run. The solid line is a one-to-one plot.

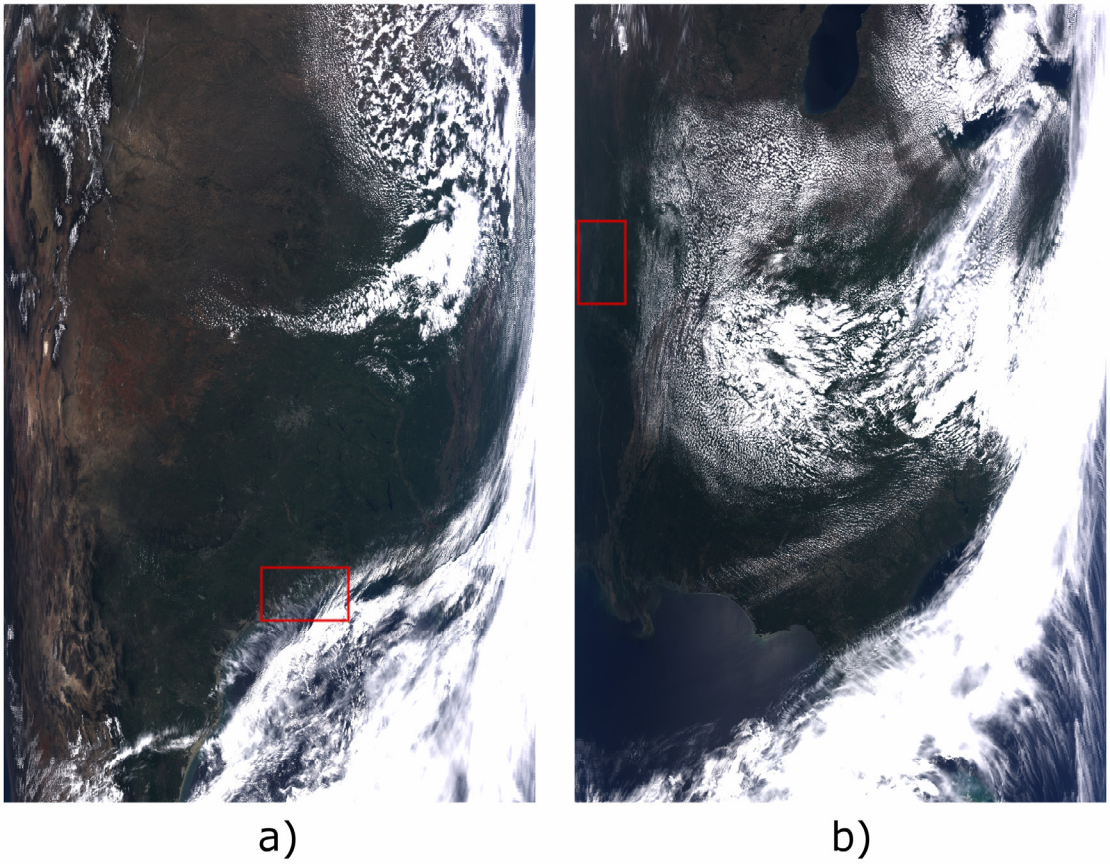

Fig. 15. False color RGB images (0.66, 0.55, and 0.47 μm) obtained from Aqua MODIS on (a) May 2, 2004, and (b) May 3, 2004. Red boxes denote the approximate regions containing WB57F spirals.

Although the WB57F flights were planned to coincide with MODIS overpass, the flight and overpass times do not precisely match. To address this issue, flight level winds observed by the aircraft are used to "advect" the flight track to its supposed location during MODIS overpass. For the May 2 case, MODIS overpass occurred roughly 30 minutes after the beginning of the spiral; for the May 3 case, MODIS overpass occurred roughly 40 minutes prior to the beginning of the spiral. It should be noted that these differences in observation times between the aircraft and MODIS may cause larger discrepancies in the observations due to changes in the clouds themselves, though the degree to which this occurs is impossible to determine.

Results from the evaluation are shown in Table 1. Listed for each case are cloud conditions at the time of aircraft observation, optical depth derived from the current method and from CLH, optical depth from the operational MODIS cloud retrievals, and specifics regarding the advected flight track and MODIS overpass. For the May 3 case, the current retrieval compares well with the CLH method. For the May 2 case, the current retrieval more closely matches the operational MODIS retrieval than the CLH.

Table 1
Evaluation results.

				WB-57										
			MODIS	Spiral Time		Latitude			Longitude			CLH	Meyer	MODIS
Date	Surface	Notes	Time	Start	End	Max	Min	Mean	Max	Min	Mean	τ	τ	τ
2004-05-02	ocean w/ no low cloud deck	spiral down	19:40	19:11	19:18	28.53	28.21	28.44	-95.80	-95.96	-95.92	4.84	3.25	3.80
2004-05-02	ocean w/ no low cloud deck	spiral up	19:40	19:18	19:26	28.42	28.22	28.32	-95.89	-96.10	-96.00	7.40	4.38	4.71
2004-05-03	SGP ARM site, no low cloud deck	spiral down	18:45	19:26	19:31	36.82	36.55	36.68	-97.65	-97.86	-97.77	0.28	0.29	0.86
2004-05-03	SGP ARM site, no low cloud deck	spiral up	18:45	19:31	19:35	36.76	36.58	36.71	-97.63	-97.91	-97.76	0.09	0.30	0.67

3.3 Summary

A method has been developed, following a simple look-up table approach, to globally retrieve ice cloud optical depth from the derived visible cirrus reflectance in the MODIS atmosphere product. This method is an update of the previous technique of Meyer et al. (2004) that limited optical depth retrieval to the tropics. For consistency with the MODIS operational retrieval algorithms, the new bulk scattering properties of ice clouds developed for the Collection 5 dataset are used here. Radiative transfer calculations revealed that visible cirrus reflectance is dependent not only on optical depth, but on ice particle effective size as well. Because of this, an effective diameter of 50 μm, corresponding to the peak in the histogram of MODIS globally derived effective particle diameters, is assumed for look-up table calculations. The applicability of the algorithm is then illustrated with two sample cases from the Aqua satellite. The algorithm is then evaluated with similar results obtained from the operational MODIS Collection 005 cloud products, as well as with in-situ aircraft observations. The main advantage of the present method is that the retrieved ice cloud optical depths are mostly attributable to upper level cirrus clouds, while both upper level cirrus clouds and lower level water clouds can sometimes contribute to the ice cloud optical depths derived from the present MODIS operational cloud algorithms.

4. ICE CLOUD STATISTICS FROM MODIS LEVEL-3 OBSERVATIONS: CLOUD OPTICAL DEPTH, ICE WATER PATH, AND FREQUENCY OF OCCURRENCE

4.1 Method

Here, simple statistics of ice cloud optical depth and ice water path, as well as ice cloud frequency of occurrence, are used to determine the spatial and temporal patterns of ice clouds. Ice cloud optical depth is derived on a global scale from the MODIS level-3 Collection 005 daily mean cirrus reflectance parameter using the method detailed in Section 3. Ice water path is calculated from the ice cloud optical depth and ice particle effective diameter. Ice cloud frequency fields are computed from cirrus reflectance parameter pixel counts.

4.1.1 Ice Water Path

Ice water path (units g m^2) is a measure of the amount of ice in a given column of the atmosphere. Here, ice water path is derived from the retrieved ice cloud optical depth as follows:

$$IWP = \frac{2\tau D_e \rho_{ice}}{3\langle Q_e \rangle}, \quad (1)$$

where τ is the retrieved ice cloud optical depth, D_e is the ice particle effective diameter, ρ_{ice} is the density of ice, and $\langle Q_e \rangle$ is the average extinction efficiency for ice at 0.66-μm. Here, we have assumed an ice particle effective diameter of 50 μm (for consistency with

the optical depth retrieval), an ice density of 917 kg m^{-3}, and an average extinction efficiency of approximately 2 (Yang et al., 2000).

4.1.2 Datasets

Data for the present study are taken from the MODIS level-3 global dataset, a daily dataset consisting of statistics computed at 1 degree spatial resolution from the MODIS level-2 1 km products. Specifically, the cirrus reflectance parameter included in the atmosphere product from both the Terra (MOD08) and Aqua (MYD08) satellites is used to create a database of daily mean ice cloud optical depth. The Terra dataset spans from February, 2000, through the present, while the Aqua dataset spans from July, 2002, through the present.

4.1.3 Statistics

The spatial and temporal trends of ice clouds are inferred from simple statistics computed from the daily mean ice cloud optical depth databases. Such simple statistics include seasonal and zonal means of optical depth and ice water path, as well as cloud frequency of occurrence. Seasonal statistics are computed for both the northern hemispheric summer (June, July, and August) and winter (December, January, and February). Here, ice cloud frequency of occurrence (F_{occ}) for each grid point is defined as follows:

$$F_{occ} = \frac{\sum_{i=1}^{n} N_{ice,i}}{\sum_{i=1}^{n} N_{tot,i}} \times 100, \qquad (2)$$

where $N_{tot,i}$ and $N_{ice,i}$ are the total and ice cloudy pixel counts (i.e., the number of pixels within each 1 degree grid box with cirrus reflectance greater than a threshold of 0.005), respectively, for day *i*. Mean ice cloud optical depth (τ_{ave}) and ice water path (IWP_{ave}), weighted with the ice cloudy pixel counts at each 1 degree grid point, are defined as

$$\tau_{ave} = \frac{\sum_{i=1}^{n}(N_{ice,i} \cdot \tau_i)}{\sum_{i=1}^{n} N_{ice,i}}, \text{ and} \tag{3}$$

$$IWP_{ave} = \frac{\sum_{i=1}^{n}(N_{ice,i} \cdot IWP_i)}{\sum_{i=1}^{n} N_{ice,i}}, \tag{4}$$

where τ_I and IWP_i are the optical depth ice water path, respectively, for day *i* at each grid point.

4.2 Results

4.2.1 Ice Cloud Frequency of Occurrence

The ice cloud frequencies of occurrence derived from Terra and Aqua for the entire four year period are shown in Fig. 16(a) and (b), respectively. Both images are scaled as indicated by the color bars at right. Note the tremendous similarities between the two images, indicating little variation between ice cloud frequencies in the morning (Terra) and afternoon (Aqua). Aqua appears to observe more ice clouds over Australia, the southern tip of Africa, and South America; however, the differences over those locations are minimal. Note also that the Inter-tropical Convergence Zone (ITCZ) is clearly visible across the center of each image, as are the storm tracks at high latitudes. Arid regions, especially mountainous regions such as the Tibetan Plateau, the Andes

Mountains in South America, and, to a lesser extent, the Rocky Mountains in the western United States, have relatively large ice cloud frequencies, a phenomenon discussed below.

Fig. 17(a) and (b) show the ice cloud frequencies of occurrence from Terra and Aqua, respectively, for the northern hemispheric summer (June, July, and August). Again, both images are scaled as shown by the color bars. Similar to Fig. 16, the morning and afternoon images are very much alike. Aqua does appear to observe a greater frequency of ice clouds over all continents; but again, differences are minimal. Here again, as in Fig. 16, arid regions are quite prominent in both images.

Fig. 18(a) and (b) show the ice cloud frequencies of occurrence from Terra and Aqua, respectively, for the northern hemispheric winter (December, January, and February). Differences again are minimal between the two images, although higher ice cloud frequencies are observed by Aqua over Africa and Australia. Note that the ITCZ in each image is farther south than in the corresponding images in Fig. 17. Arid regions are again easily visible in both images.

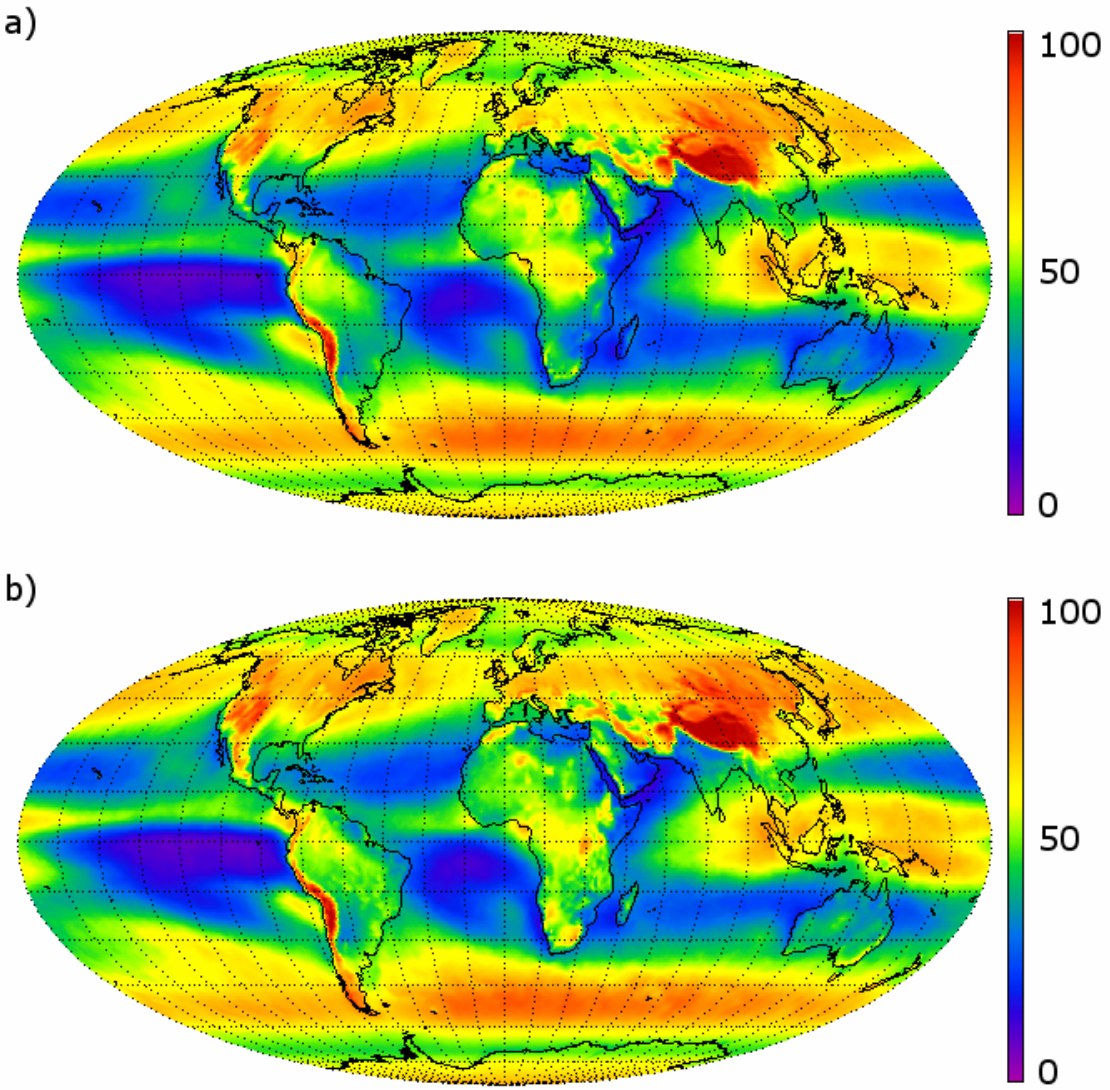

Fig. 16. Ice cloud frequency of occurrence derived from the MODIS cirrus reflectance parameter for the entire seven year period of Terra (a) and four year period of Aqua (b).

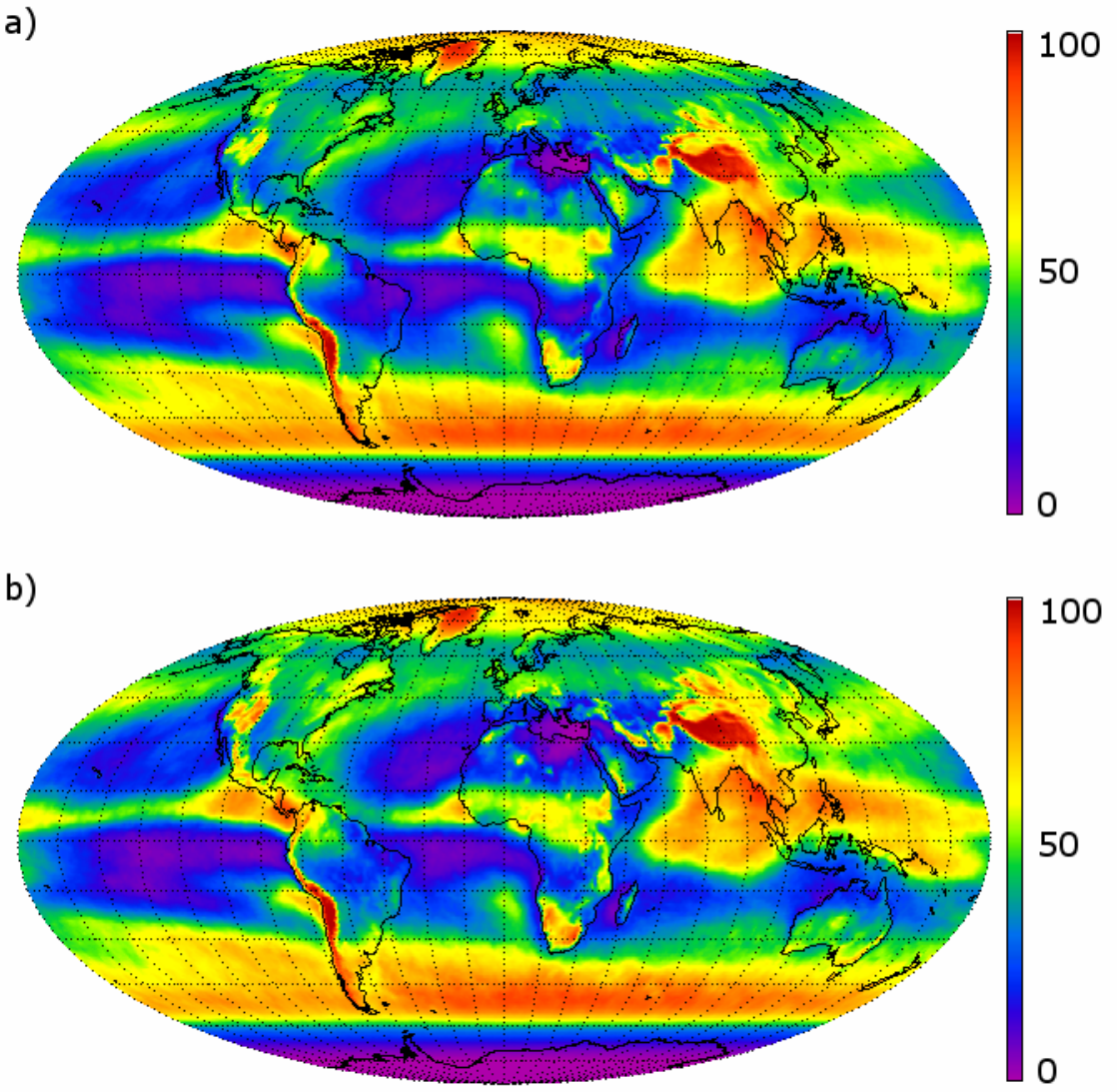

Fig. 17. Northern hemispheric summer (June, July, August) ice cloud frequency of occurrence derived from the MODIS cirrus reflectance parameter for Terra (a) and Aqua (b).

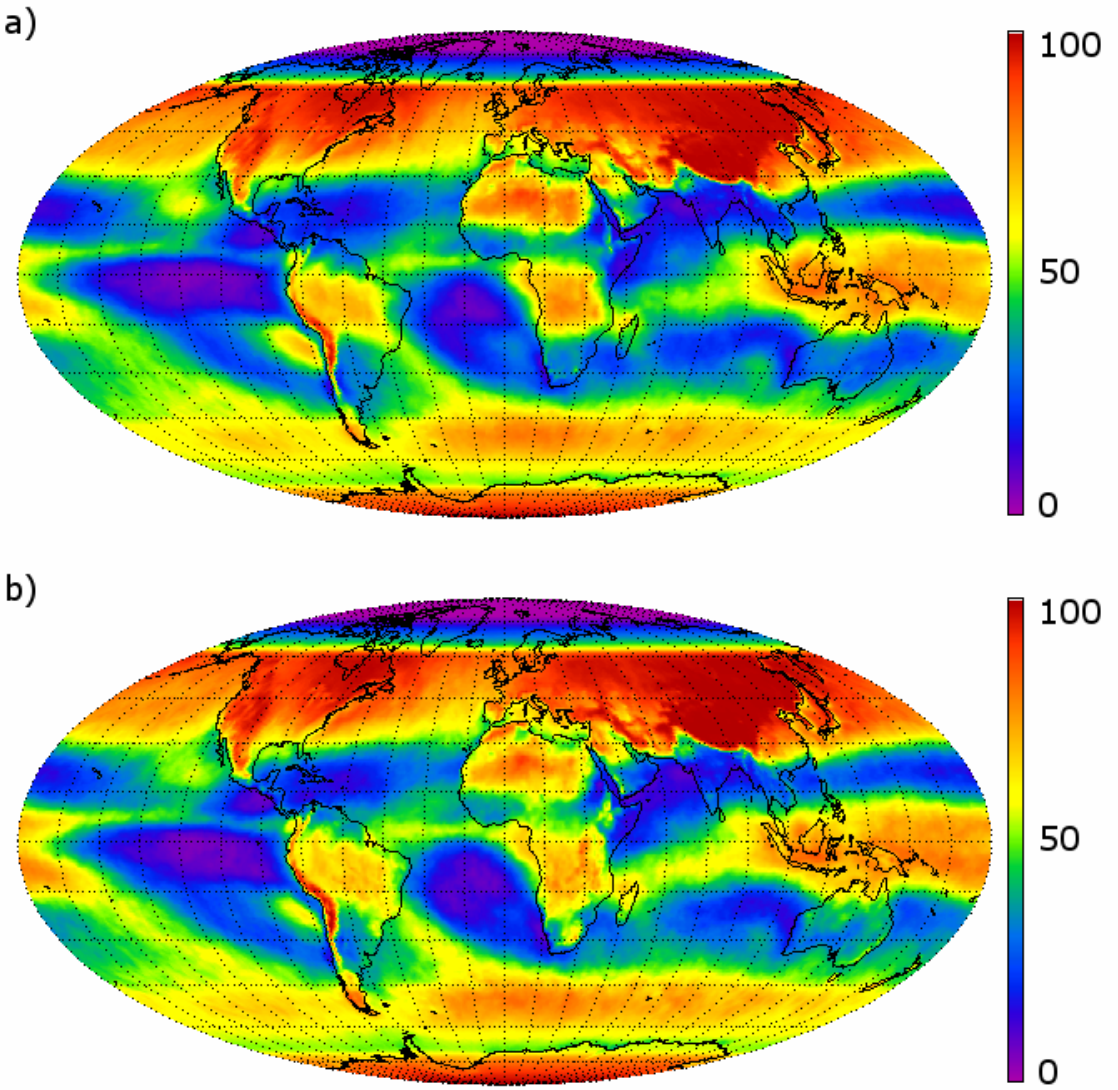

Fig. 18. Northern hemispheric winter (December, January, February) ice cloud frequency of occurrence derived from the MODIS cirrus reflectance parameter for Terra (a) and Aqua (b).

The relatively high ice cloud frequencies observed over arid regions, such as the Andes Mountains, Rocky Mountains, and the Tibetan Plateau, as well as over northern Africa during the winter (Fig. 18), may be attributable to surface contamination of the 1.375 μm channel. Surface contamination can result from a lack of water vapor in the atmosphere sufficient enough to absorb all incident and reflected 1.375 μm radiation. Analyses of water vapor images taken from MODIS reveal very low amounts of water vapor over mountainous regions, such as the Andes and Himalayas, and desert regions, such as the Sahara in northern Africa (especially prominent during the winter months). Fig. 19 shows the MODIS atmospheric water vapor (i.e., cm of precipitable water) measured from the Aqua platform for (a) the entire four year period, (b) the summer months, and (c) the winter months. Note the relatively low values (less than 1 cm) over the regions listed above. The incomplete removal of signals leaked into the 1.375-μm channel from other wavelengths during the MODIS radiometric calibration processes can also contribute to the large frequency of "cirrus reflectance" over northern Africa.

Zonally averaged ice cloud frequency of occurrence for both Aqua (solid lines) and Terra (dotted lines) MODIS is shown in Fig. 20. Red lines indicate the northern hemispheric summer months, blue lines indicate northern hemispheric winter months. Note the local maxima near the equator, denoting the ITCZ. As expected, these maxima are further south during the winter. The local maxima near the poles are quite large. This can be attributed in part to actual ice cloud coverage, but also to surface contamination in the 1.375 μm channel, as there is an abundance of surface ice and snow (high albedo) coupled with a relatively dry atmosphere.

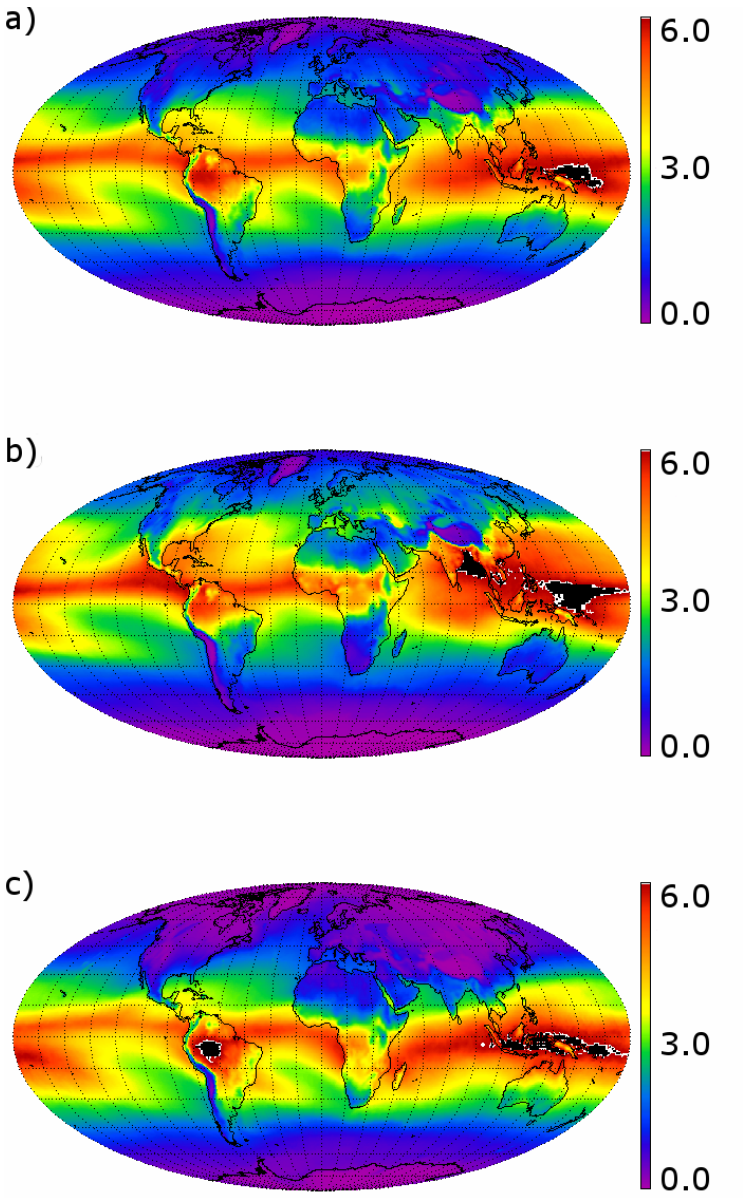

Fig. 19. Atmospheric water vapor (cm) from the operational Aqua MODIS atmosphere product. (a) Mean water vapor for the entire four year period. (b) Mean water vapor for the northern hemispheric summer months. (c) Mean water vapor for the northern hemispheric winter months.

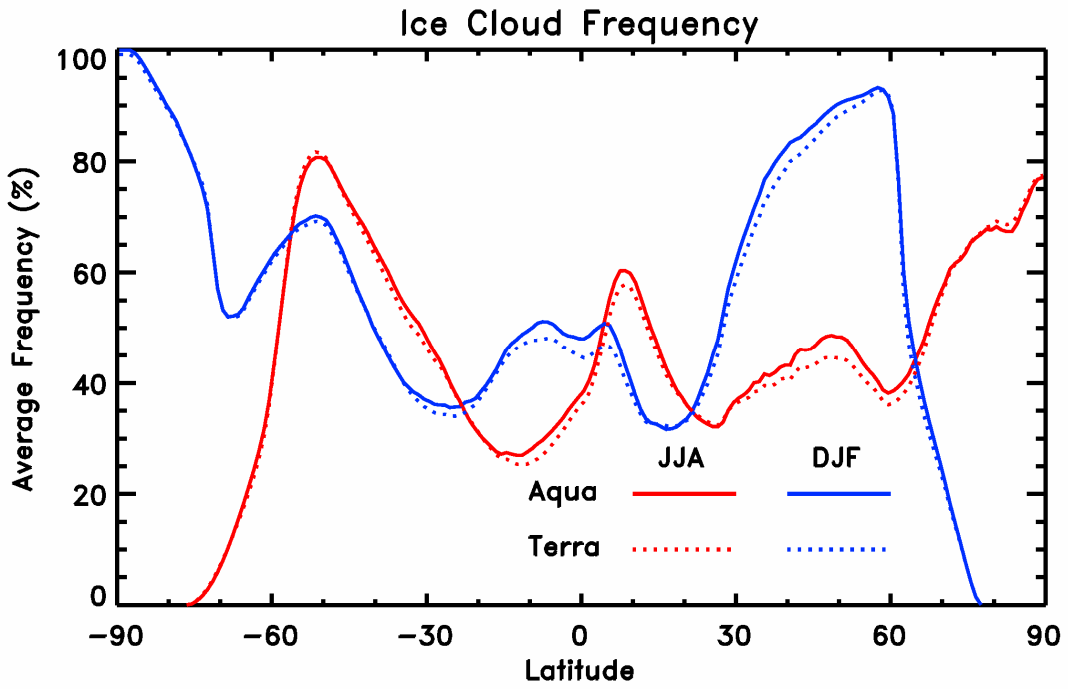

Fig. 20. Zonally averaged ice cloud frequency of occurrence from the MODIS on Aqua (solid line) and Terra (dotted line). Red indicates the northern hemispheric summer (June, July, and August), blue indicates the northern hemispheric winter (December, January, and February).

4.2.2 Ice Cloud Optical Depth

Daily mean ice cloud optical depth has been calculated using the entire observational period of the MODIS. Fig. 21 shows histograms of the daily mean ice cloud optical depths for both the Terra (solid) and Aqua (dotted) datasets. The histograms are nearly identical, though Terra MODIS does observe slightly more thin ice clouds than Aqua MODIS, a phenomenon evident in the following figures. Note that the histograms are extremely right skewed, with a vast majority of daily mean optical depths below 5.0 (more specifically, approximately 95% of Terra and 94% of Aqua MODIS observations fall below this threshold). The distribution appears to be from the gamma family (of which the lognormal distribution is included). Missing data accounts for approximately 27% of both the Terra and Aqua data.

Mean ice cloud optical depth for the entire observational period is shown in Fig. 22 for both Terra (a) and Aqua (b). Both images are scaled as indicated by the color bars at right. The patterns observed in each plot are remarkably similar. However, Aqua observes optically thicker clouds than Terra over the continents, most notably over South America, the middle of Africa, and throughout Asia. The ITCZ is clearly visible across the center of each image, as are the storm tracks at higher latitudes.

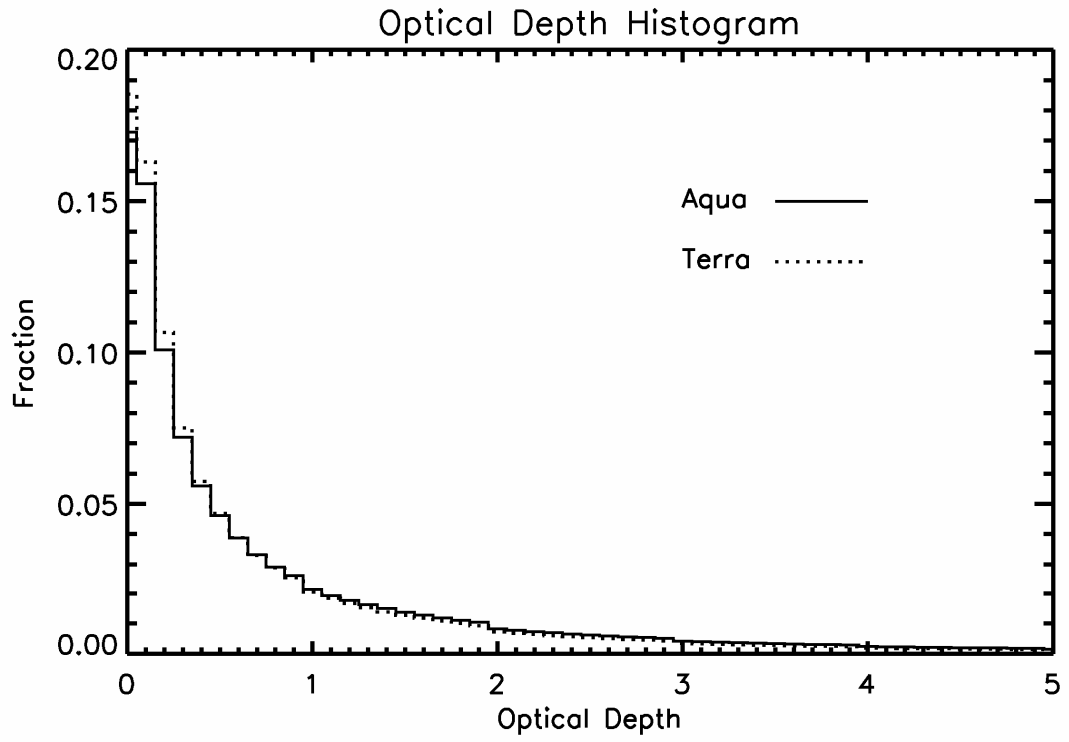

Fig. 21. Histograms of daily mean optical depths obtained from the entire observational periods of Terra (dotted line) and Aqua (solid line).

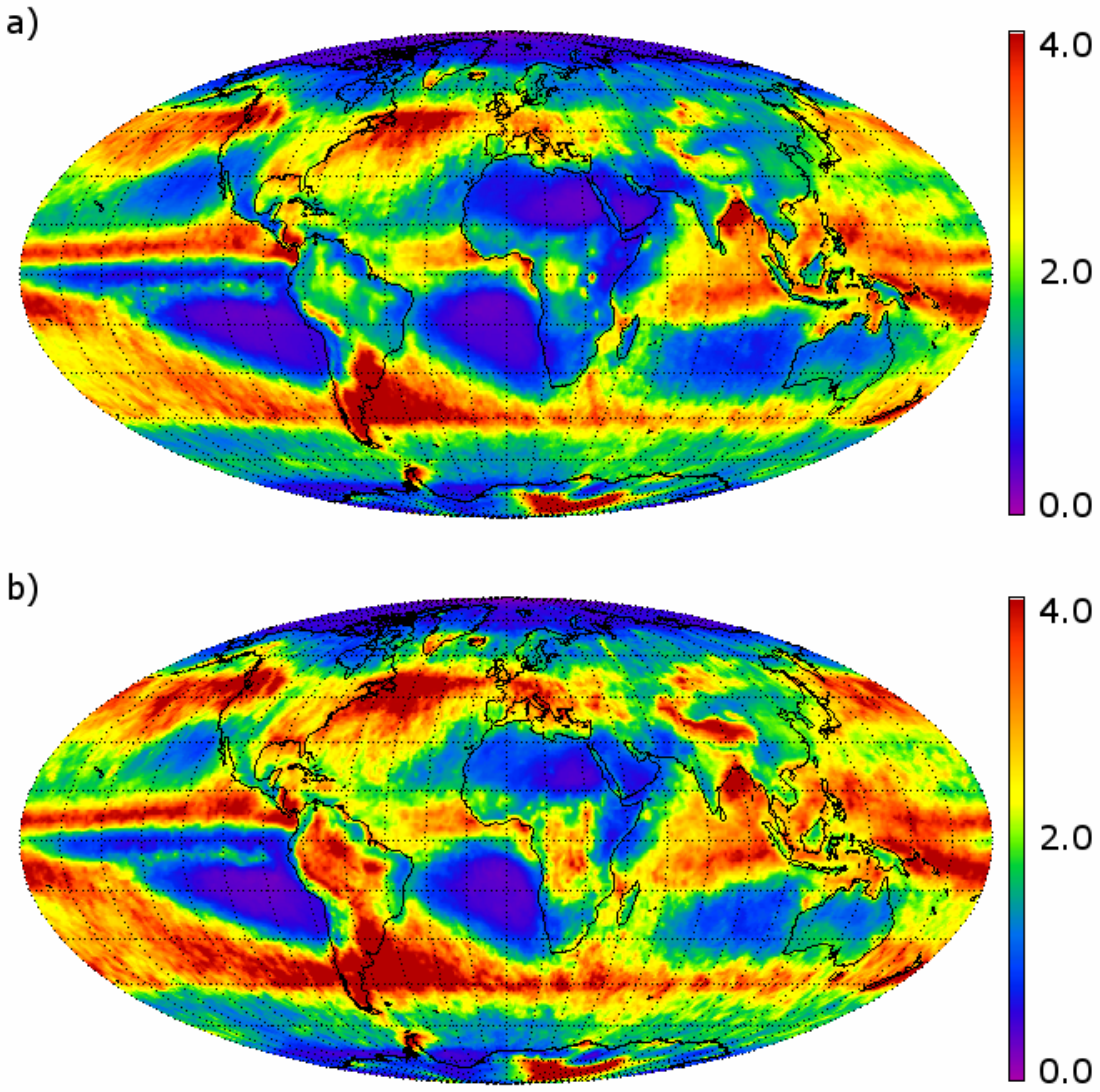

Fig. 22. Mean ice cloud optical depth for the entire period of (a) Terra and (b) Aqua MODIS observations.

Fig. 23 shows the mean ice cloud optical depth for the summer months (June, July, and August) obtained from Terra (a) and Aqua (b) MODIS. The ITCZ is quite evident across the center of each image. Note also that Aqua observes optically thicker clouds than Terra. This difference is most notable over the continents, especially North and South America, Europe, and Asia. Increased convection during the afternoons most likely contributes to the increased optical depths observed by Aqua MODIS.

Fig. 24 shows the mean ice cloud optical depth for the winter months (December, January, and February) obtained from Terra (a) and Aqua (b) MODIS. Similar to Fig. 23, Aqua MODIS observes optically thicker ice clouds than Terra MODIS and, again, this difference is most evident over continents, specifically in the southern hemisphere (South America, Africa, and Australia). There also appears to be slightly larger optical depths surrounding Antarctica in the Aqua image. Again, increased convection in the afternoons most likely contributes to these differences.

Zonally averaged daily mean ice cloud optical depths for both Terra (dotted lines) and Aqua (solid lines) MODIS are shown in Fig. 25. Red indicates the northern hemispheric summer months, blue indicates the northern hemispheric winter months. Similar to Fig. 20, note the local maxima (ITCZ) near the equator. Again, as expected, these maxima are further south during the winter months. Also note the large peaks over mid-latitudes, phenomena readily visible in Fig. 23 and 24. Increased activity within the storm tracks during local winter most likely contributes to these peaks. Overall, Aqua MODIS observes optically thicker clouds than Terra MODIS, although the differences generally are not considerable.

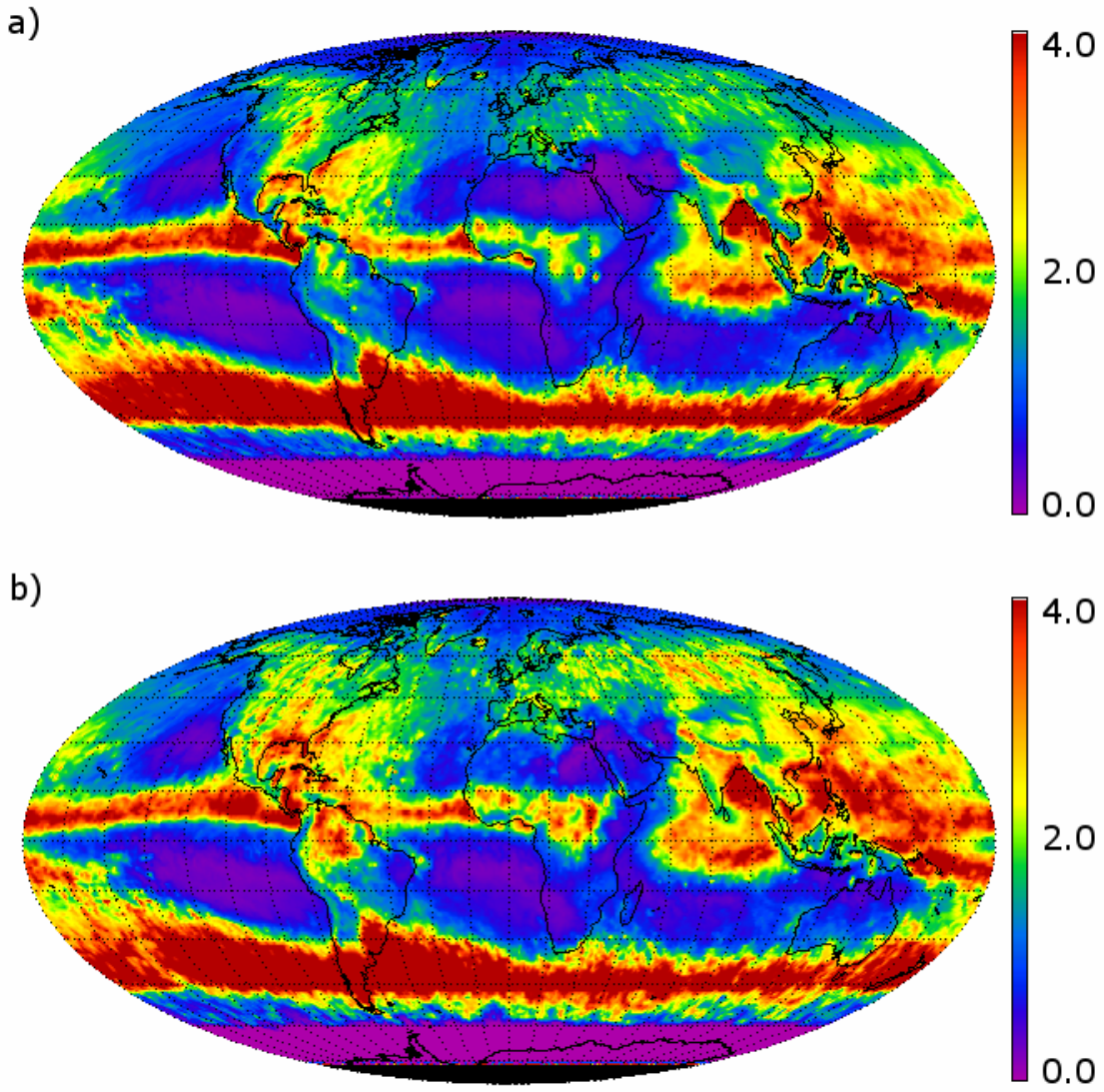

Fig. 23. Mean ice cloud optical depth for the summer months (June, July, and August) obtained from Terra (a) and Aqua (b) MODIS.

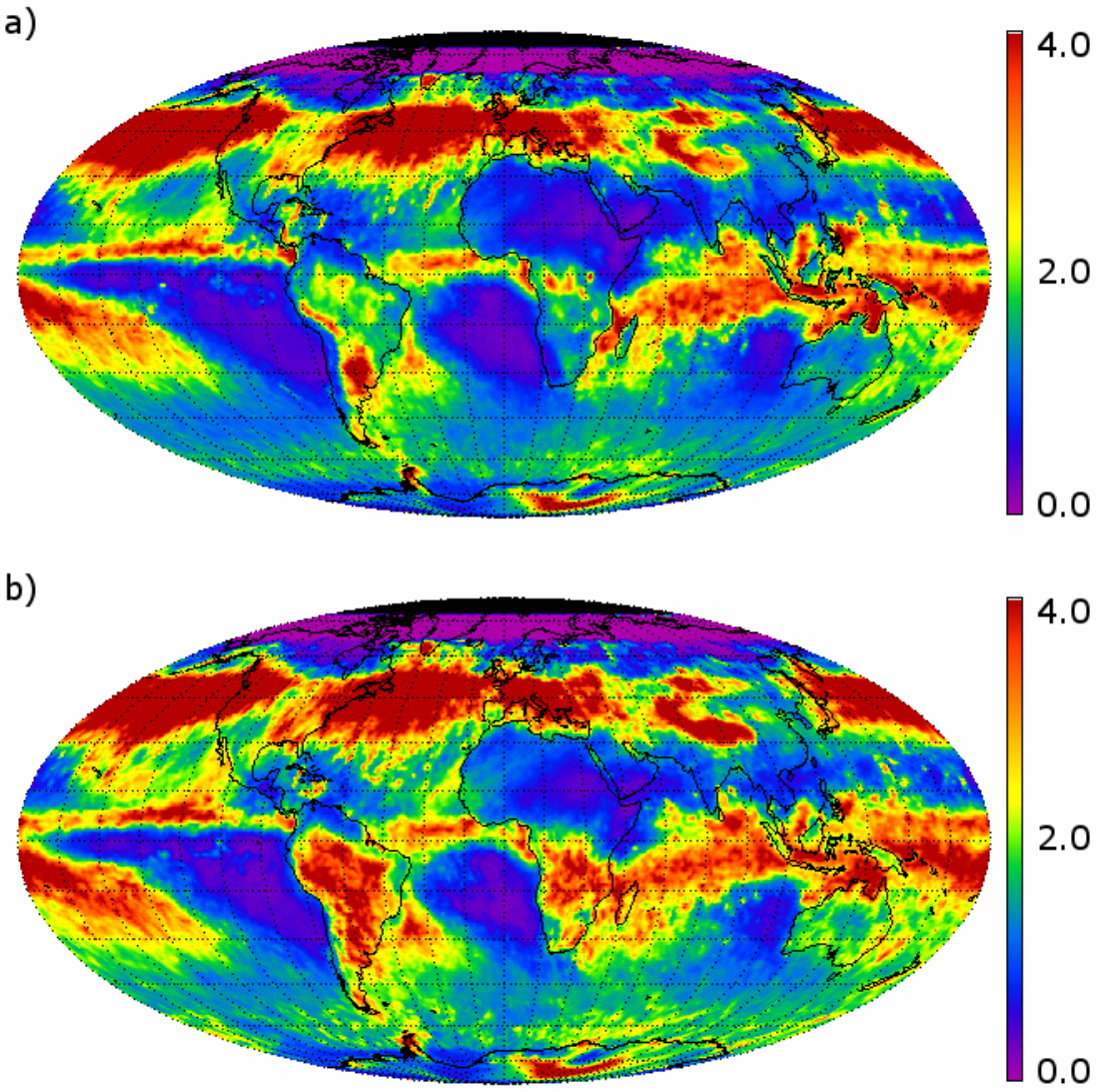

Fig. 24. Mean ice cloud optical depths for the winter months (December, January, and February) obtained from Terra (a) and Aqua (b) MODIS.

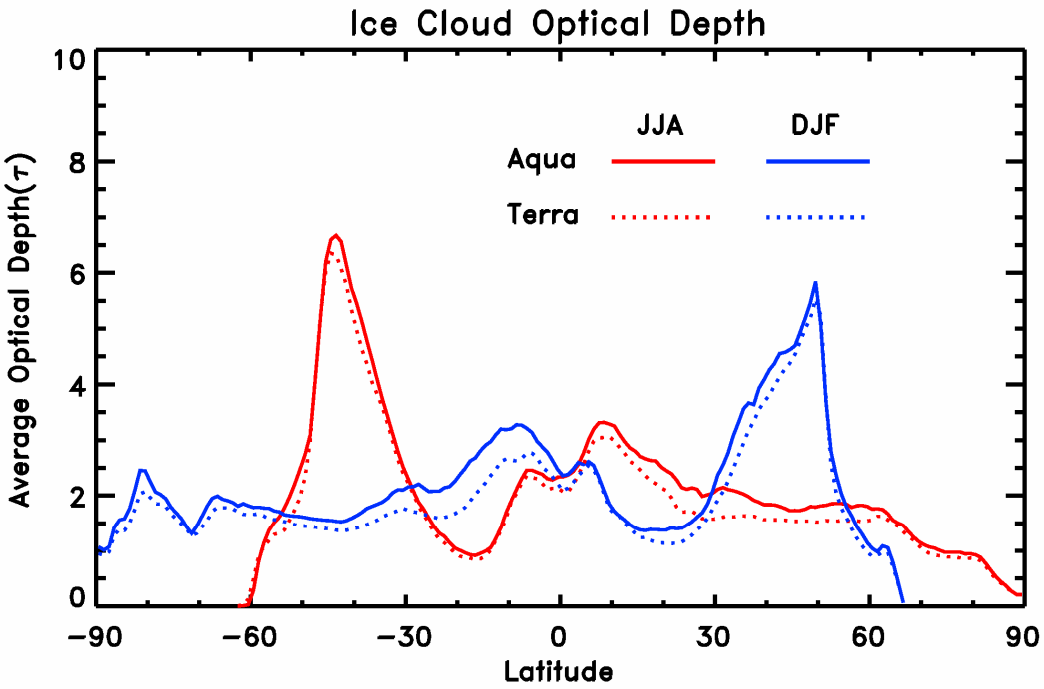

Fig. 25. Zonally averaged daily mean ice cloud optical depth from Aqua (solid lines) and Terra (dotted lines) MODIS. Red indicates the summer months (June, July, and August), blue indicates the winter months (December, January, and February).

4.2.3 Ice Water Path

Daily mean ice water path is calculated from Equation 4 for the entire observational periods of Aqua and Terra MODIS. Histograms of these values for both Terra (dotted line) and Aqua (solid line) are shown in Fig. 26. Similar to the optical depth histograms in Fig. 21, Terra MODIS observes small ice water paths more frequently than Aqua MODIS. Both histograms are extremely right-skewed, with 92% (90%) of Terra (Aqua) MODIS observations less than 50 g m^2. Here, missing data accounts for approximately 27% of both datasets.

Fig. 27 shows the mean ice water path for the entire observational periods of both Terra (a) and Aqua (b) MODIS. Both images are scaled as indicated by the color bars at right. Both images show remarkable similarities in pattern; however, Aqua MODIS observes larger ice water paths than Terra MODIS, most notably over the continents, but also off the northeast coast of North America as well as the southeast coasts of South America and Africa.

Fig. 28 shows the mean ice water path from Terra (a) and Aqua (b) MODIS for the northern hemispheric summer months (June, July, and August). Again, the observable spatial patterns in both images show remarkable similarities. Aqua MODIS does observe larger ice water paths, particularly over the northern hemispheric continents and the northern portion of South America.

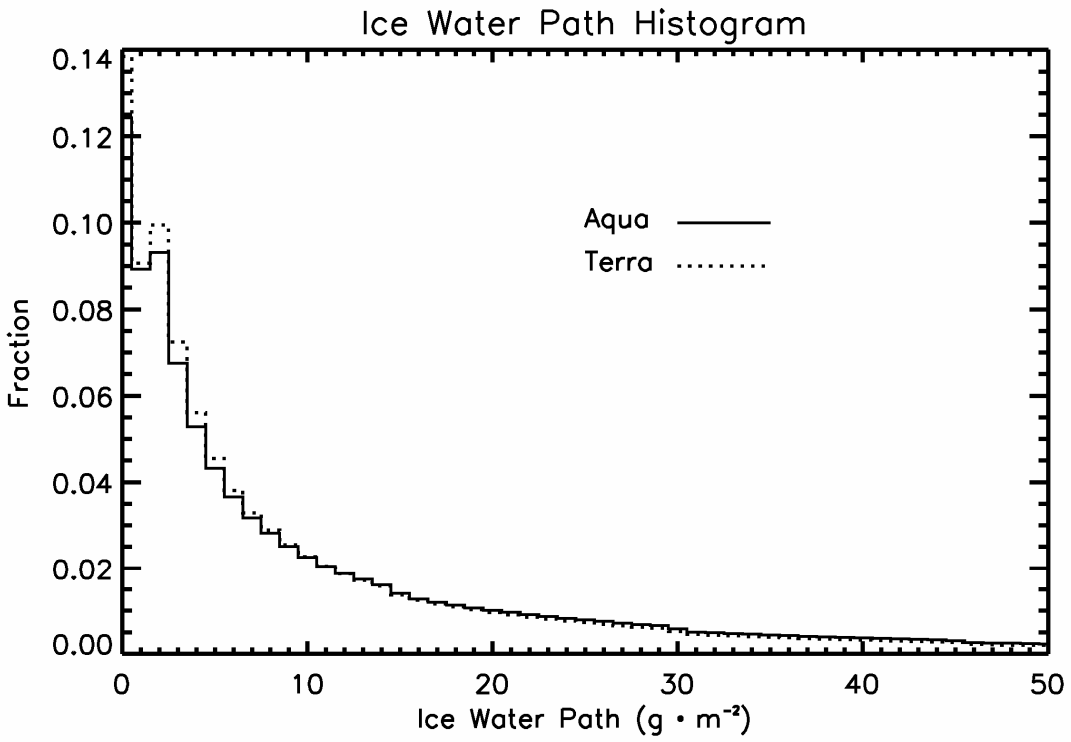

Fig. 26. Histograms of ice water path derived from the entire observational periods of Terra (dotted line) and Aqua (solid line) MODIS.

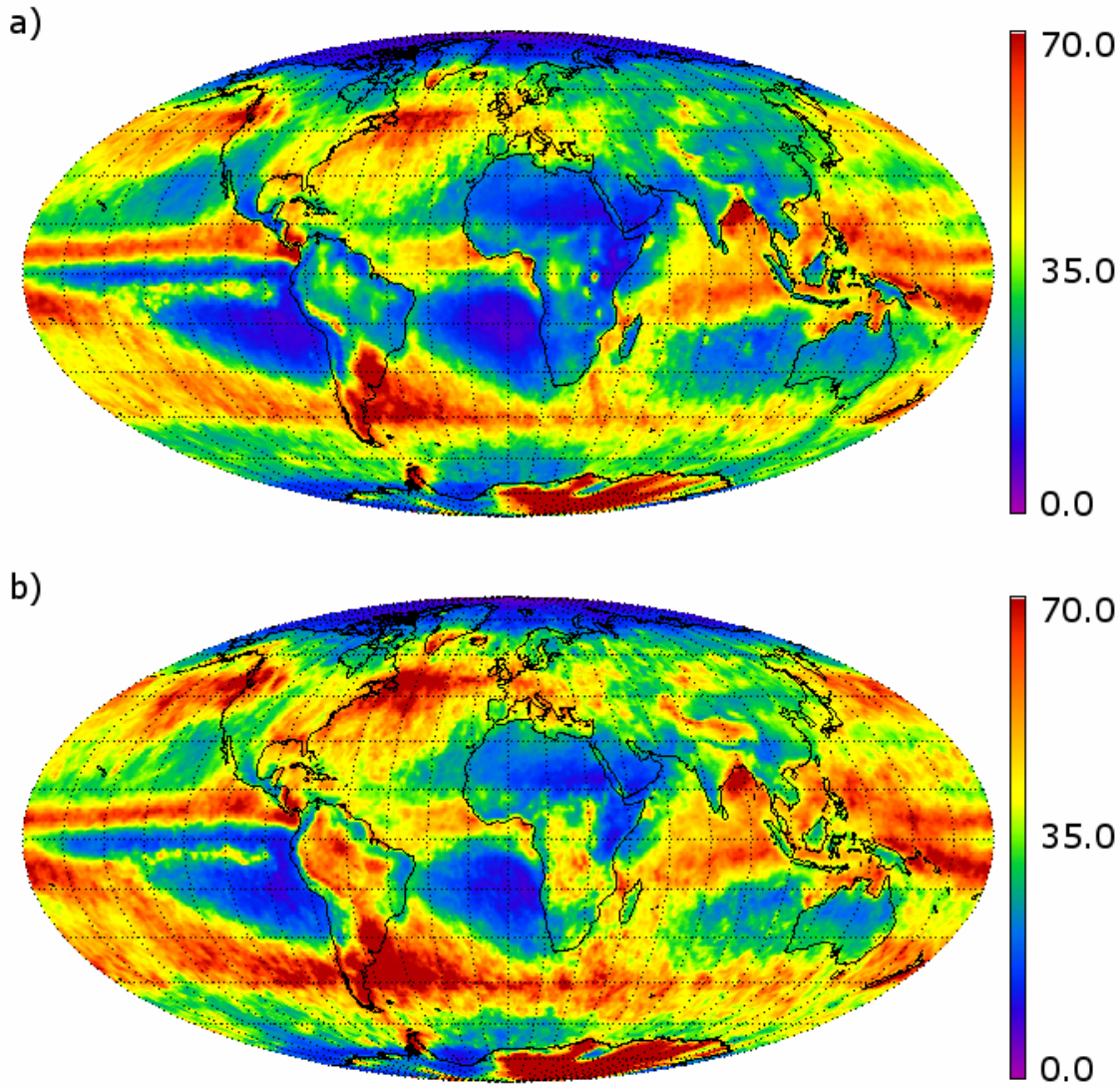

Fig. 27. Mean daily ice water path from the entire observational periods of both Terra (a) and Aqua (b).

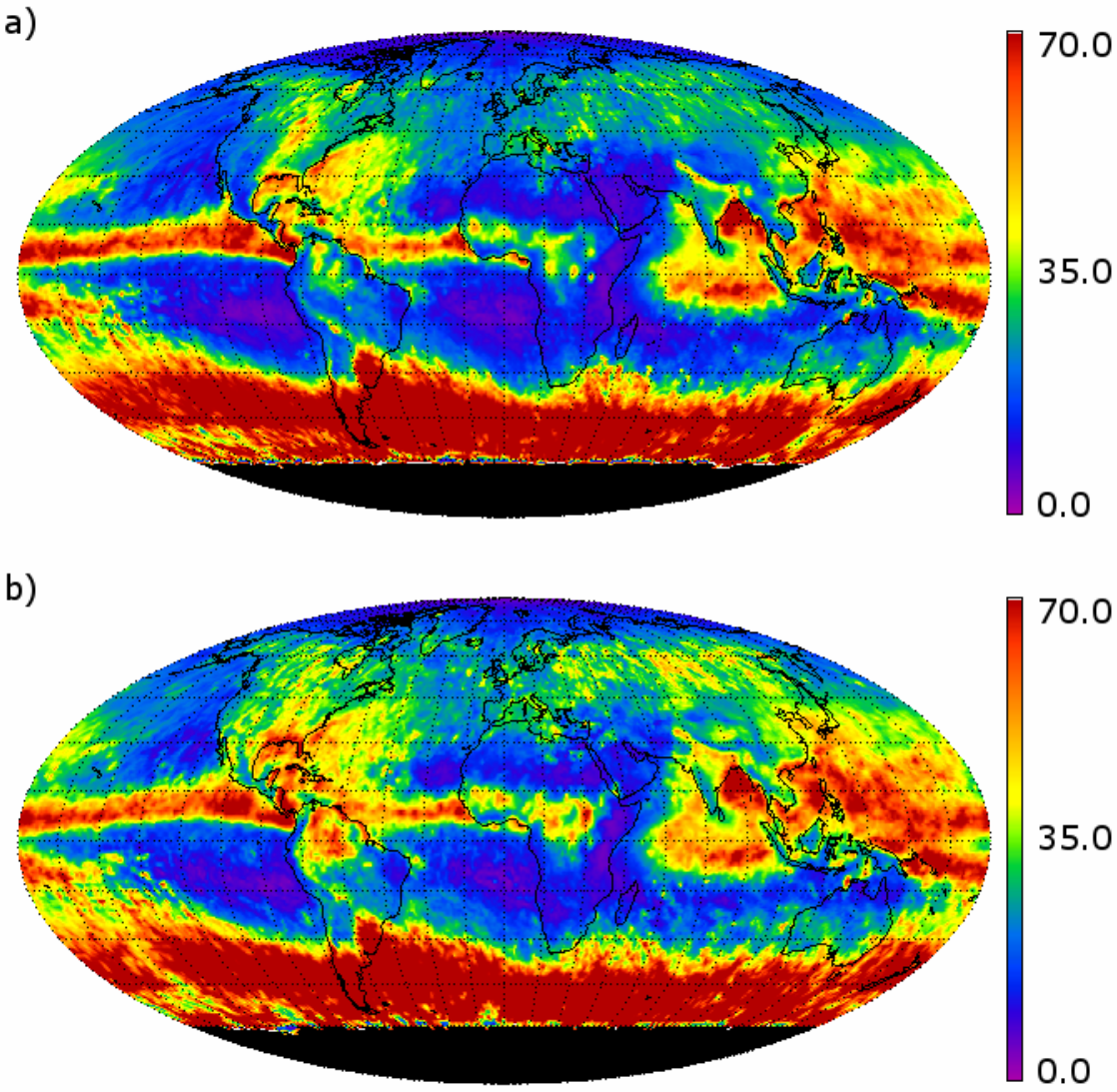

Fig. 28. Mean daily ice water path observed by (a) Terra and (b) Aqua MODIS for the northern hemispheric summer months (June, July, and August).

Fig. 29 shows the mean ice water path from Terra (a) and Aqua (b) MODIS for the northern hemispheric winter months (December, January, and February). The patterns observed in both images show significant similarities, although, again, Aqua MODIS observes larger ice water paths. These differences are most notable over the southern hemispheric continents, specifically South America, southern Africa, and Australia.

Zonally averaged daily mean ice water path is shown in Fig. 30 for both Terra (dotted lines) and Aqua (solid lines) MODIS. Here, red indicates the northern hemispheric summer months, blue indicates the northern hemispheric winter months. The local maxima near the equator, which result from the ITCZ, are further north during the summer months than during the winter months, as expected. The larger peaks over higher latitudes, corresponding to the storm tracks, are quite visible in preceding figures. The general pattern is identical to that shown in the zonal optical depth plot (Fig. 25), which is to be expected under the assumptions made in Equation 4. In general, Aqua MODIS observes larger ice water paths compared to Terra MODIS.

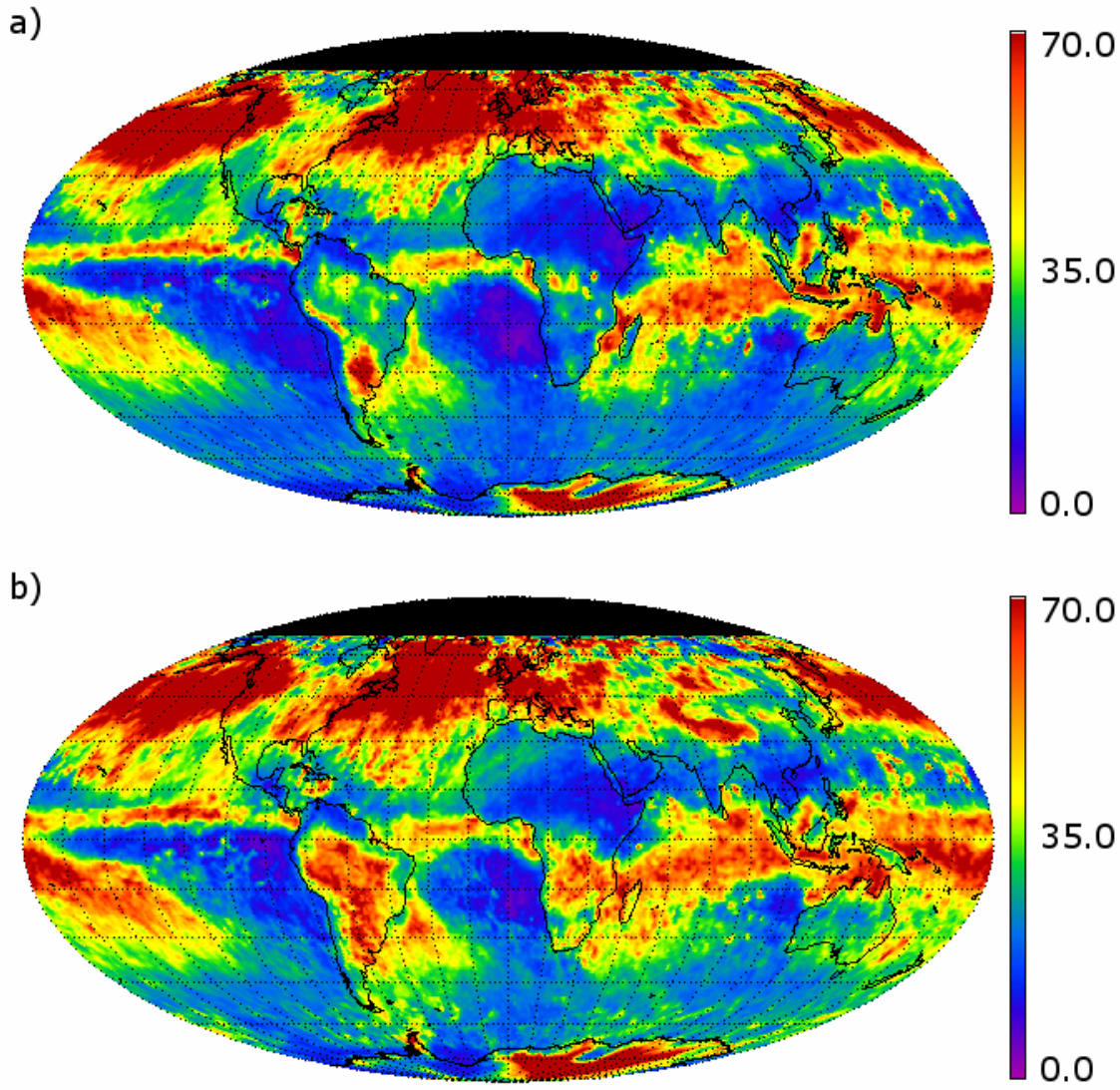

Fig. 29. Mean daily ice water path observed by (a) Terra and (b) Aqua MODIS for the northern hemispheric winter months (December, January, and February).

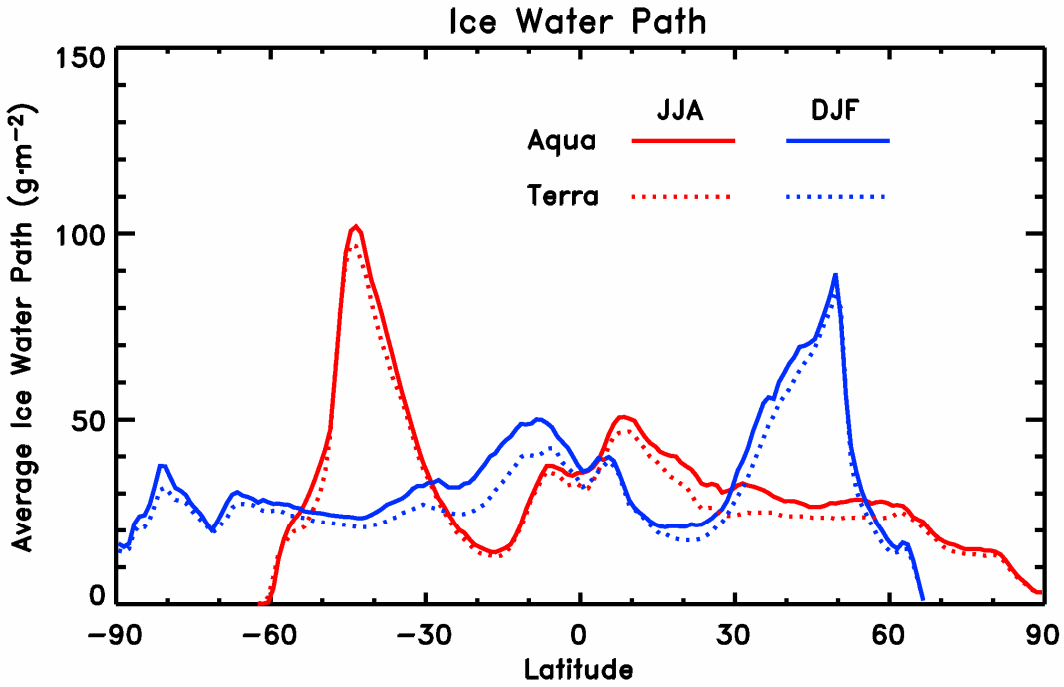

Fig. 30. Zonally averaged daily mean ice water path observed by Terra (dotted lines) and Aqua (solid lines) MODIS. Red indicates the northern hemispheric summer months (June, July, and August), blue indicates the northern hemispheric winter months (December, January, and February).

4.2.4 Global Trends

Global time trends of various atmospheric parameters, such as temperature and cloud cover, can be, and often are, used to describe and understand broad changes in the Earth's ever-evolving climate. Here, global ice cloud trends are investigated to determine how these clouds have changed over time. Ice clouds are particularly interesting due to their effects on the Earth's radiative budget. It has been suggested that cirrus clouds have a positive net radiative forcing (i.e., a warming effect on the atmosphere), although clouds with a large number of small ice crystals have a negative net forcing (Zhang et al., 1999).

Fig. 31 shows the global time trends of the mean monthly ice cloud frequency of occurrence obtained from Terra (blue line) and Aqua (red line) MODIS observations. Fig. 31(a) is the trend averaged over the entire earth, while (b) and (c) are the northern and southern hemispheric trends, respectively. Note the Terra dataset starts a year and a half before the Aqua dataset. Trend lines are plotted for the Terra dataset only. Ice cloud frequency appears to by quite cyclical, as global minima occur each year in late northern hemispheric summer. Also, there is no significant trend in frequency, as trend slopes are essentially zero. Overall, Aqua MODIS observes ice clouds slightly more frequently than Terra MODIS.

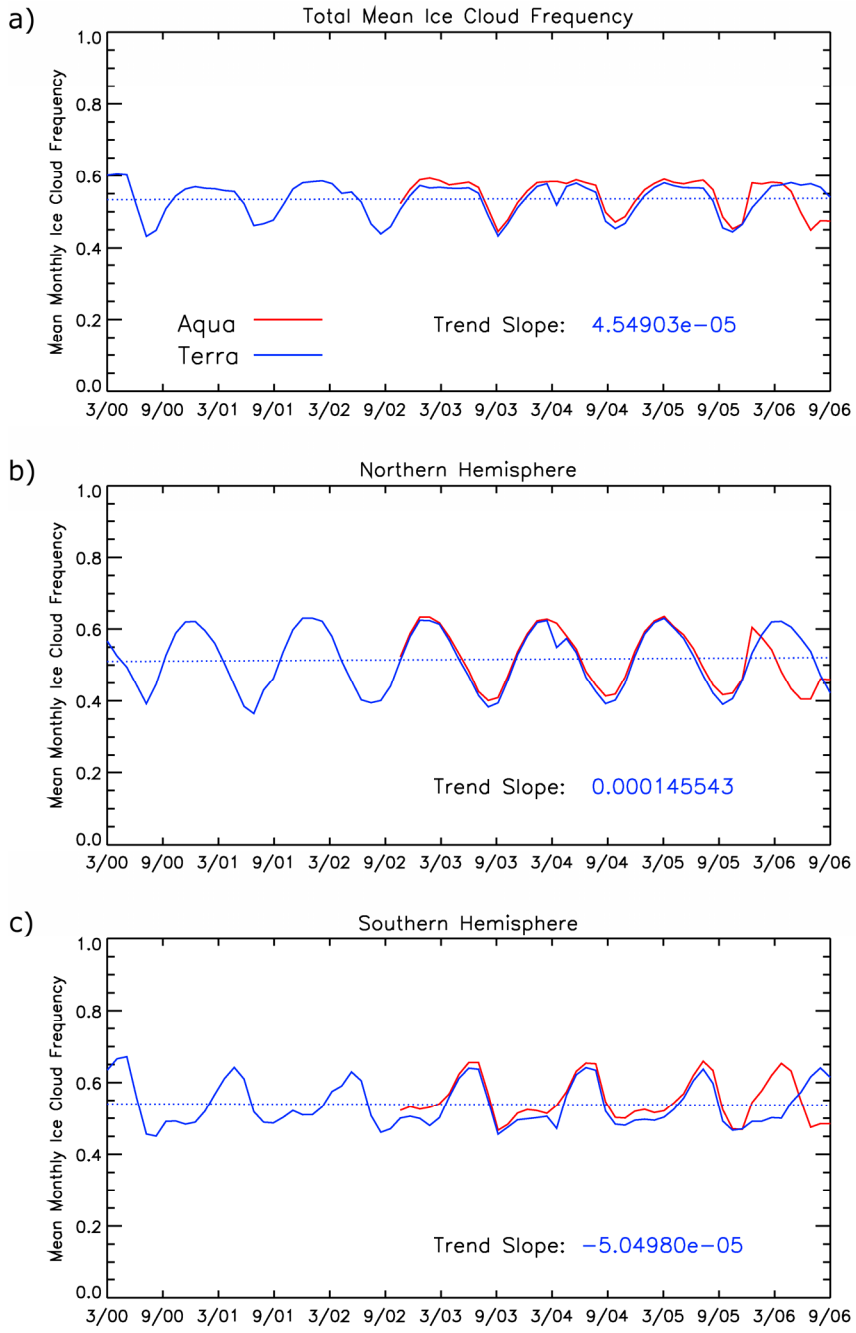

Fig. 31. Time trends of mean ice cloud frequency of occurrence obtained from Terra (blue line) and Aqua (red line) MODIS observations. The slopes of the trend lines corresponding to the Terra plots are shown.

Fig. 32 shows the global time trends of the mean monthly ice cloud optical depth derived from Terra (blue) and Aqua (red) MODIS observations. Fig. 32(a) is the trend averaged over the entire earth, and (b) and (c) are the trends averaged over the northern and southern hemispheres, respectively. Again, trend lines are plotted for Terra MODIS only. Similar to ice cloud frequency, ice cloud optical depth is quite cyclical, although here it exhibits bi-annual fluctuations, with global maxima during the northern hemispheric winter and summer. Here, too, Aqua MODIS observes optically thicker clouds than does Terra MODIS. Again, similar to ice cloud frequency, there is no overall trend in the Terra dataset (although the northern hemispheric plot does show a slight downward trend, mostly due to decreasing maxima).

Fig. 33 shows the global time trends of the mean monthly ice water path derived from Terra (blue) and Aqua (red) MODIS observations. Once more, (a) is the trend averaged over the entire earth, and (b) and (c) are the trends averaged over the northern and southern hemispheres, respectively. Trend lines are plotted for the Terra MODIS dataset only. The cyclical nature of ice water path follows that of ice cloud optical depth, namely, global maxima during the northern hemispheric winter and summer. Here, yet again, Aqua MODIS observes slightly larger ice water path than does Terra MODIS. However, global ice water path does exhibit a slight downward trend, mostly due to a decrease by nearly 4 g m^{-2} in the northern hemisphere plot.

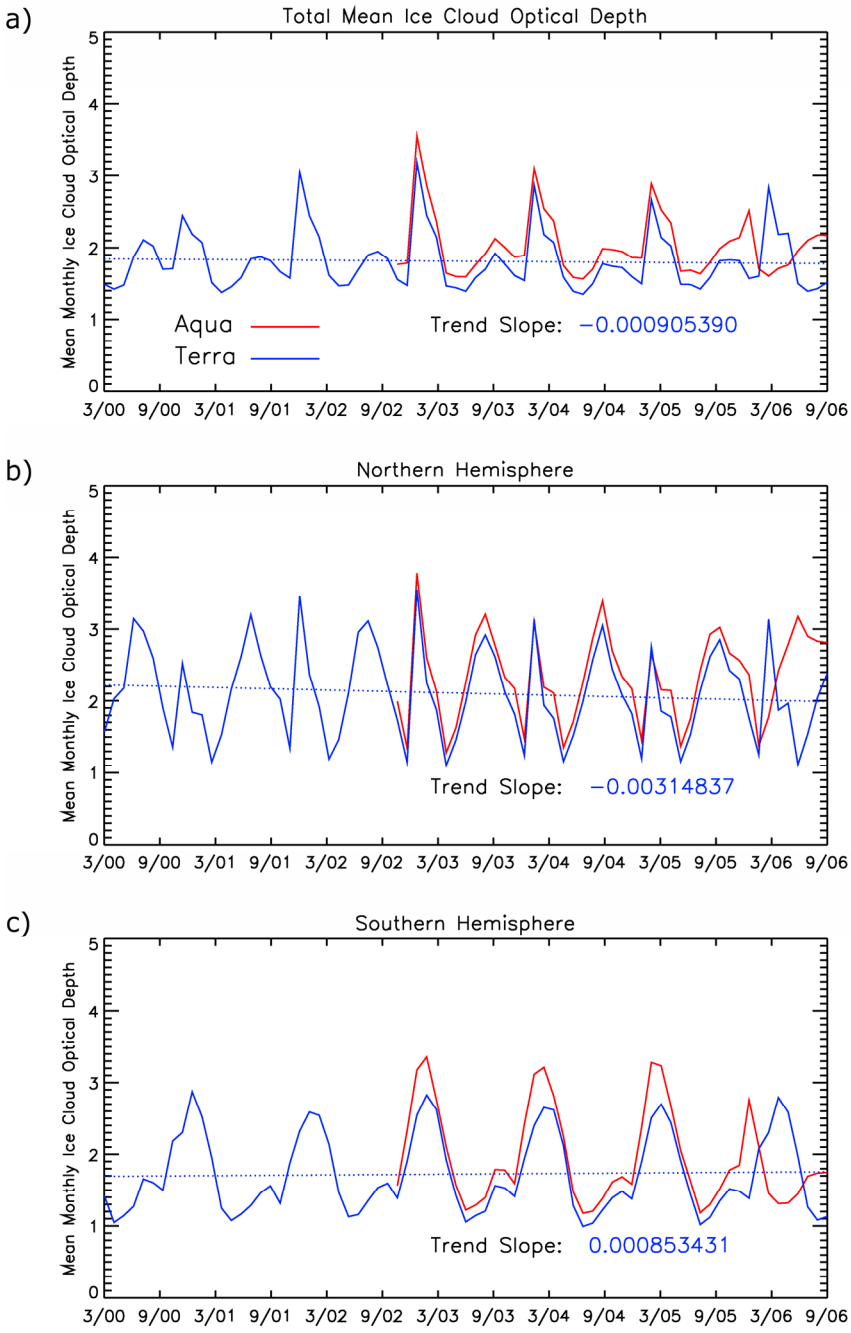

Fig. 32. Time trends of mean ice cloud optical depth derived from Terra (blue) and Aqua (red) MODIS observations. The slopes of the trend lines corresponding to the Terra plots are shown.

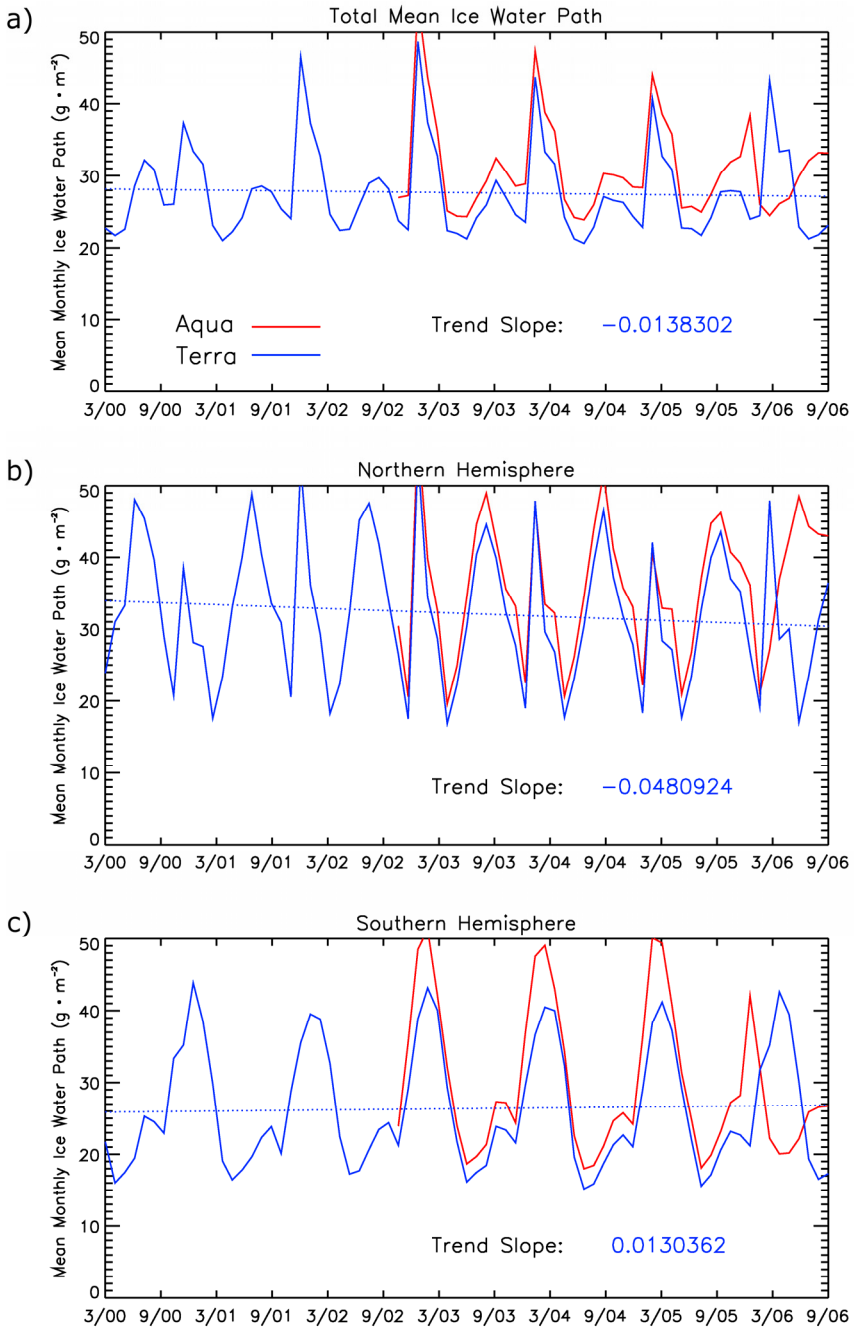

Fig. 33. Time trends of mean ice water path derived from Terra (blue lines) and Aqua (red lines) MODIS observations. The slopes of the trend lines corresponding to the Terra plots are shown.

4.3 Summary

Here, an analysis of global ice clouds has been completed using simple statistics of daily ice cloud observations from the level-3 MODIS atmosphere product. Frequency of occurrence, mean ice cloud optical depth (derived from the technique in Section 3), and mean ice water path are determined for the entire observational periods of Terra and Aqua MODIS, as well as for the northern hemispheric summer and winter seasons. It has been found that ice clouds occur quite frequently near the equator and at high latitudes. Also Aqua MODIS consistently observes more frequent ice clouds, higher cloud optical depth, and larger ice water path than Terra MODIS, although the differences between the two are relatively small. Globally averaged ice cloud frequency, optical depth, and ice water path reveal seasonal fluctuations, but no significant trend throughout either dataset.

5. TIME SERIES ANALYSIS OF DAILY ICE CLOUD OPTICAL DEPTH

Here, ice cloud patterns are investigated from a global perspective using a time series analysis of daily optical depth measurements obtained from the MODIS on board NASA's Aqua satellite. The statistical analysis follows the method of Cahalan et al. (1982), who analyzed cloud patterns using diurnal observations of outgoing infrared (IR) radiance measured by the NOAA satellites. The focus of Cahalan et al. (1982) is a time series analysis of the IR radiance using correlation calculations. Autocorrelation provides insight into the persistence of cloud patterns, and cross-correlation provides insight into the movement and persistence of cloud patterns through both space and time.

5.1 Method

Daily ice cloud optical depth time series are derived, using the technique detailed in Section 3, from four years (Sep. 2002 through Sep. 2006) of the Aqua MODIS Collection 005 level-3 cirrus reflectance parameter. The level-3 dataset, a global product on a $1^{\circ} \times 1^{\circ}$ (360×180 grid points) horizontal grid, contains statistically averaged parameters from the level-2 dataset (1km spatial resolution at nadir). The derived optical depths are archived according to date.

5.1.1 Missing Data

The MODIS was designed to view the entire globe within one to two days. However, due to orbital geometry and swath width, the MODIS is unable to completely view the tropics within this time frame. This shortcoming ultimately results in gaps, or missing data, in the dataset. Fig. 34(a) shows a sample time series taken from Aqua MODIS over the western Pacific Ocean. Fig. 34(b) shows a magnification of the blue section of the time series in (a). Missing data are denoted by gaps in the time series. Orbital precession causes the missing data gaps to shift position from day to day, such that any given location within the tropics is not dominated by missing data. This is evident in Fig. 34(b). Nevertheless, these missing data must be properly accounted for when performing statistical time series analyses.

A number of methods currently exist to properly account for missing data. Such methods include simple mean insertion, deletion, and techniques base on maximum likelihood estimators. Rankin and Marsh (1985) found that the deletion method, in which missing data are simply omitted from the time series, does not alter the meaning of a time series when missing data accounts for less than 20% of the dataset. From a cursory analysis of MODIS cirrus reflectance observations, it has been found that missing data accounts for approximately 5-10% of any given time series over the tropics, a region which, excluding the polar regions, contains a majority of the missing data. Consequently, the deletion method should hold for the current analysis.

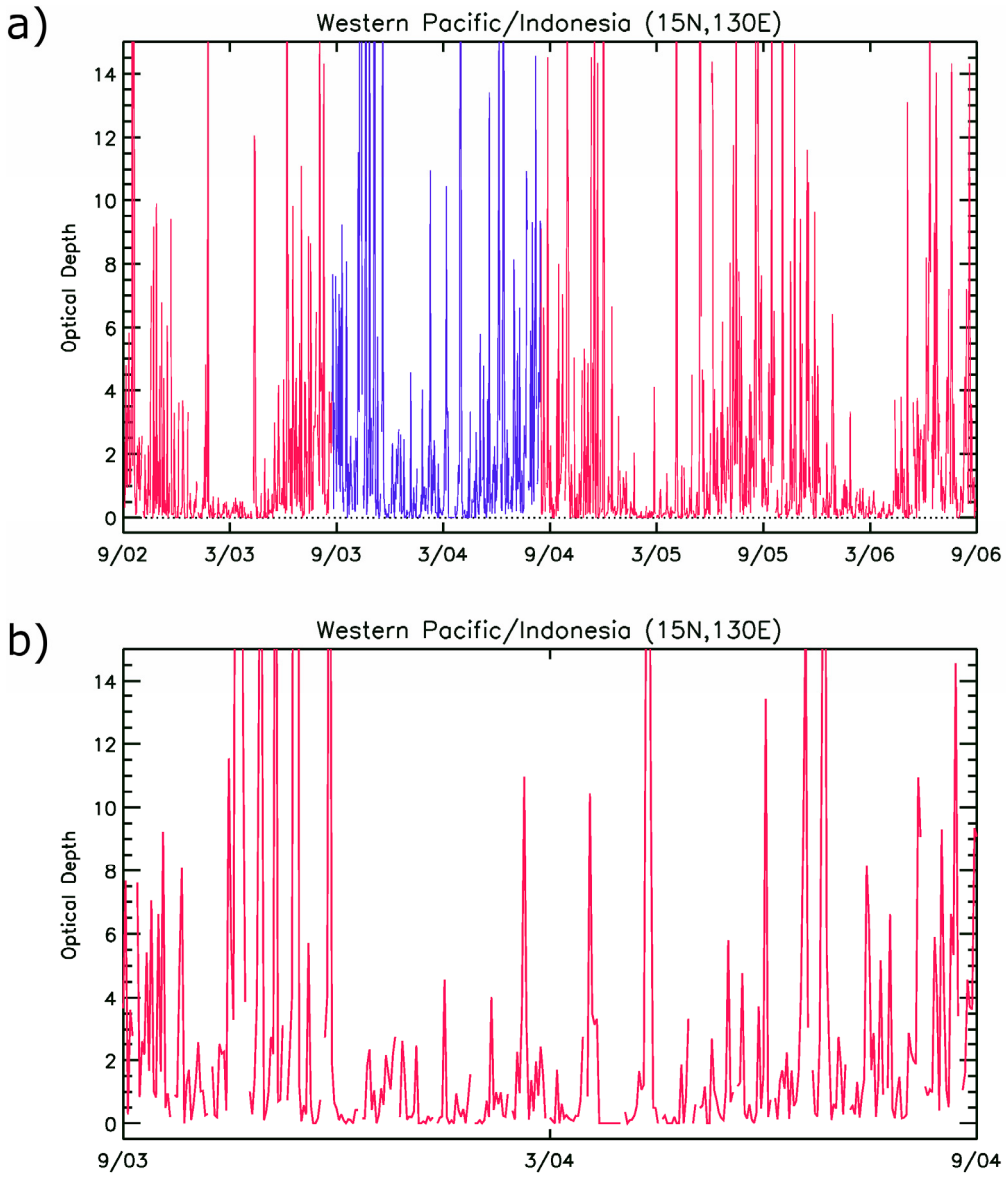

Fig. 34. Sample time series of daily optical depths derived from Aqua MODIS observations over the western Pacific Ocean. (a) Daily time series for the entire observational period. (b) Magnification of the blue section of the time series in (a). Breaks in the plot denote missing data.

5.1.2 Data Seasonality and Non-Normality

The validity of any time series analysis is directly dependent on the characteristics of the dataset itself. Often, certain characteristics can lead to less than desired results. For instance, long-scale fluctuations in the dataset, often referred to as seasonality, may dominate the analysis, concealing the underlying small-scale fluctuations. Of somewhat greater importance, however, is the shape of the distribution of the dataset. Most common statistical tools are applicable only under the assumption of normality, i.e., the dataset is distributed symmetrically with mean zero and standard deviation one. Results from time series analyses of datasets that do not meet this criterion are difficult to evaluate, and may be meaningless.

Seasonality is quite evident in long datasets of cloud observations, and the present ice cloud optical depth observations are no exception. The most common seasonality is associated with the Intertropical Convergence Zone (ITCZ). The ITCZ, seen as the band of relatively widespread convective clouds near the equator, gradually moves between hemispheres throughout the year, following the seasonal movement of the sun (with respect to the Earth) from the southern hemisphere during northern hemispheric winter to the northern hemisphere during the summer. Subsequently, locations near the equator experience alternating periods of increased and decreased cloud cover. Fig. 35 illustrates the seasonality of ice cloud optical depth observations over the Atlantic Ocean (latitude 5°S, longitude 15°W).

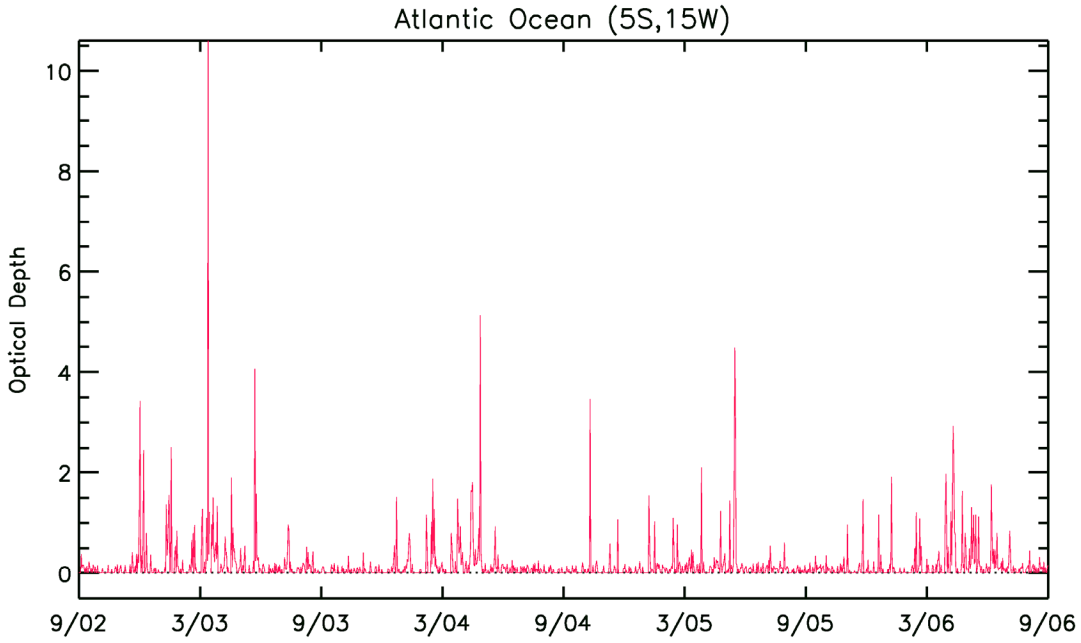

Fig. 35. Time series of daily optical depth values derived from Aqua MODIS observations over the Atlantic Ocean (latitude 5°S, longitude 15°W). Note the seasonality exhibited by the time series (increased optical depths during local spring).

Because the present study focuses on analyses of daily fluctuations of optical depth, the seasonality of the dataset should be removed. This can be accomplished by means of the boxcar average (or moving average) technique. The boxcar average, *BA*, about a given optical depth observation at location x, τ_x, is calculated as follows:

$$BA_{\tau_x} = \frac{\sum_{i=x-n}^{x+n} \tau_i}{2n+1}, \tag{5}$$

where $2n+1$ denotes the total number of observations included in the average. For instance, to calculate the boxcar average using the 10 observations surrounding a given value in the time series, use $n = 5$. Seasonality is then removed by subtracting each boxcar average value from its corresponding optical depth observation. In the present study, a 31-day ($n = 15$) boxcar average is used.

Fig. 36(a) shows the time series in Fig. 35 plotted with the 31-day boxcar average (blue line). Note the seasonality of the series is quite evident in the boxcar average plot. Subtracting the boxcar average from the time series yields the residual series shown in Fig. 36(b). Note here that the magnitude of the residual time series still increases during local spring; however, there is no general increasing or decreasing trend.

Fig. 37 shows the histogram of the residual time series in Fig. 36(b). Evidently, the boxcar average method not only removes seasonality, but also transforms the dataset into a semi-symmetric distribution (optical depth is extremely right-skewed, as illustrated by Fig. 21). Even though the series is still not Gaussian, the symmetry of the distribution should be sufficient for the time series analysis.

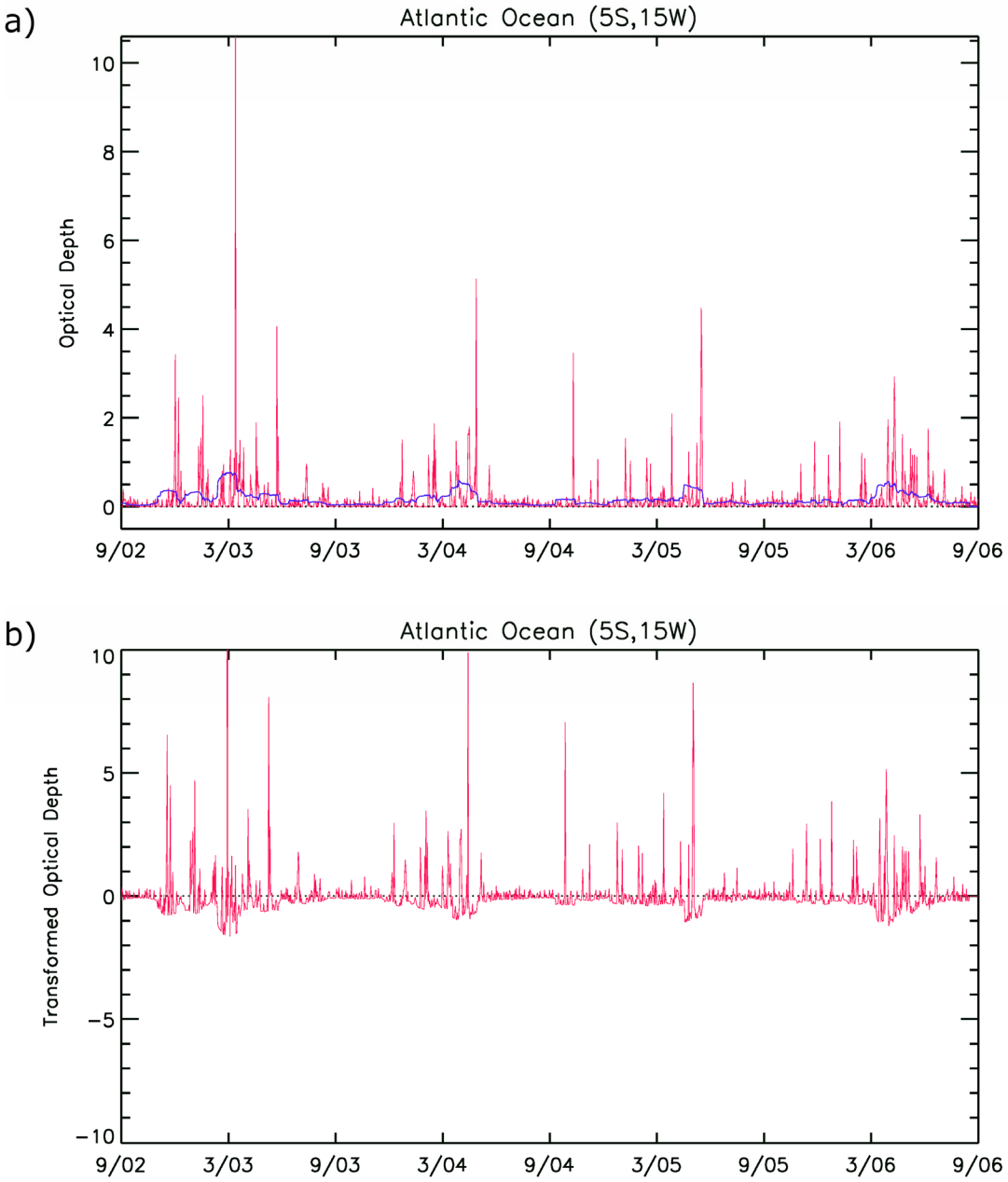

Fig. 36. Example of the boxcar average method. (a) Time series from Fig. 35 (red line) plotted with the 31-day boxcar average (blue line). (b) Residual time series resulting from subtracting the boxcar average from the time series.

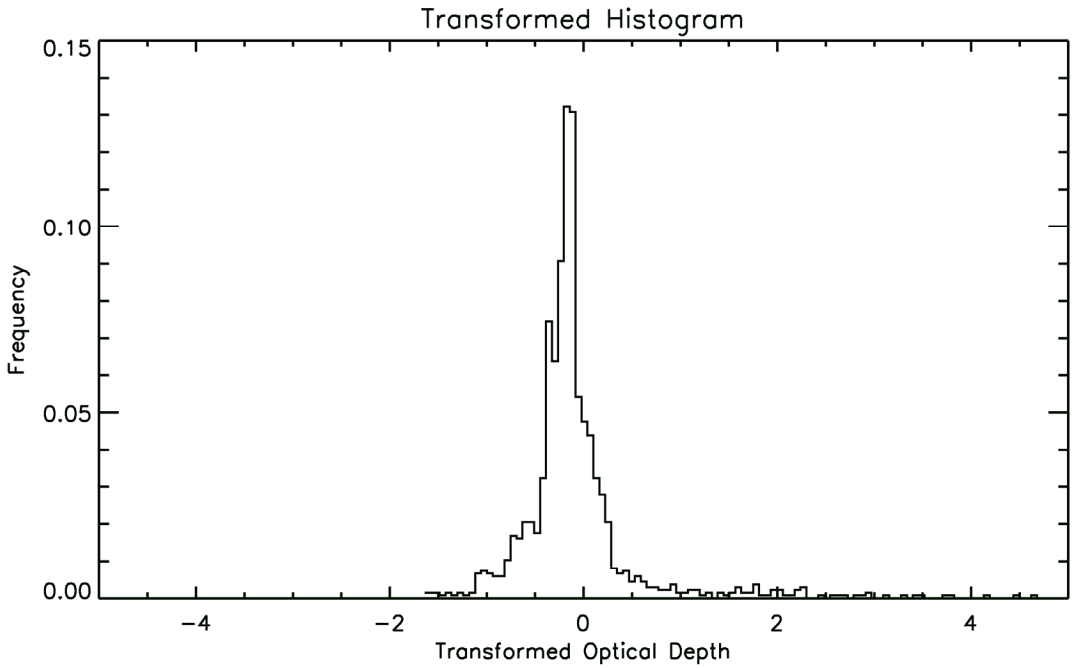

Fig. 37. Histogram of the residual time series shown in Fig. 36(b). Note the symmetry of the distribution. This is in stark contrast to the right-skewed gamma distribution of optical depth.

5.1.3 Correlation

The present time series analysis employs correlation calculations to determine, statistically speaking, the persistence and movement of ice clouds. These calculations are carried out at each 1˚ × 1˚ MODIS level-3 grid point. Autocorrelation gives a measure of how well a given time series compares to a time-shifted version of itself as a function of the time shift, or lag day. In terms of the present study, it provides a measure of the persistence of an ice cloud pattern over a given location. Autocorrelation is calculated using the intrinsic Interactive Data Language (IDL) function *a_correlate*, which defines autocorrelation as

$$P_\tau(L) = \frac{\sum_{i=0}^{N-L-1}(\tau_i - \bar{\tau})(\tau_{i+L} - \bar{\tau})}{\sum_{i=0}^{N-1}(\tau_i - \bar{\tau})^2}, \qquad (6)$$

where $P_\tau(L)$ is the autocorrelation at lag day L, N is the time series length, and $\bar{\tau}$ is the time series mean. Autocorrelation values range from -1 to 1, with 1 denoting perfect correlation, and -1 denoting perfect anti-correlation. The lag day L can be any integer (when $L = 0$, the autocorrelation function is 1). When autocorrelation falls below $1/e$ (~0.37), the time series is said to have no "memory" of itself, indicating the pattern observed in the original time series does not persist. A sample autocorrelation plot, corresponding to the residual time series in Fig. 36(b), is shown in Fig. 38. Note that autocorrelation falls below $1/e$ within one day, indicating little persistence of ice clouds over this location.

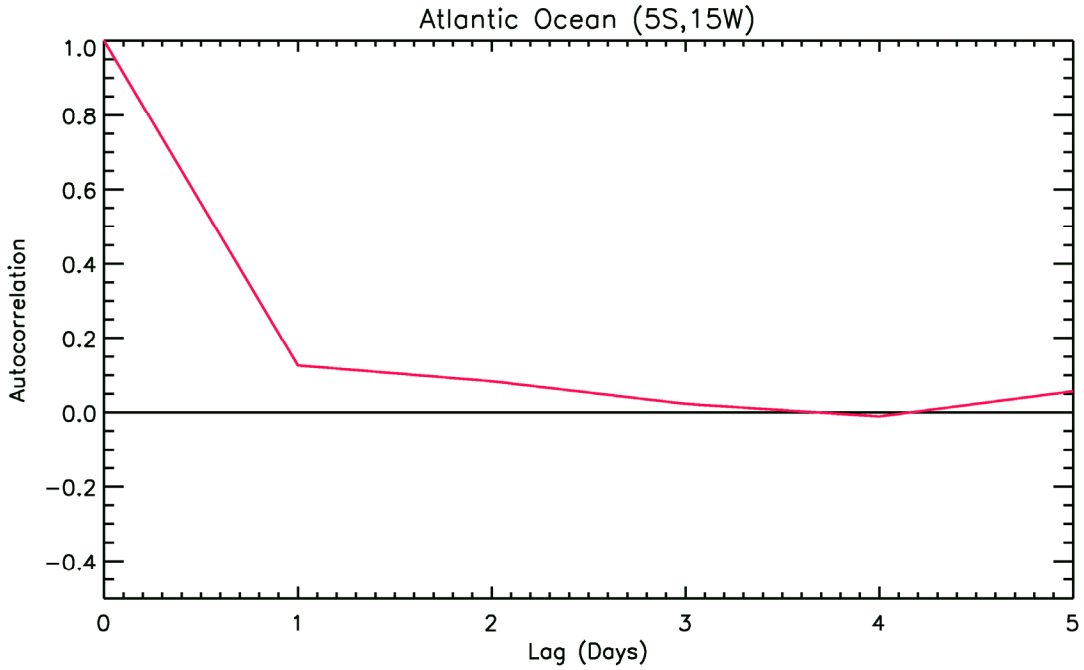

Fig. 38. Sample autocorrelation plot corresponding to the residual time series in Fig. 36(b). Here, autocorrelation falls below 1/*e* within one day, indicating little ice cloud persistence.

Similar to autocorrelation, cross-correlation provides a measure of how a given time series compares to a second time-shifted time series. It can be used to determine the persistence in time, as well as the movement through space, of observable ice cloud patterns. Here, cross-correlation is calculated using the intrinsic IDL function *c_correlate*, which defines cross-correlation as

$$P_{\tau}(L) = \begin{cases} \dfrac{\sum_{i=0}^{N-|L|-1}(\tau_{i+|L|} - \bar{\tau})(\eta_i - \bar{\eta})}{\sqrt{\left[\sum_{i=o}^{N-1}\left(\tau_i - \bar{\tau}\right)^2\right]\left[\sum_{i=o}^{N-1}\left(\eta_i - \bar{\eta}\right)^2\right]}} & For\ L < 0 \\ \dfrac{\sum_{i=0}^{N-L-1}(\tau_i - \bar{\tau})(\eta_{i+L} - \bar{\eta})}{\sqrt{\left[\sum_{i=o}^{N-1}\left(\tau_i - \bar{\tau}\right)^2\right]\left[\sum_{i=o}^{N-1}\left(\eta_i - \bar{\eta}\right)^2\right]}} & For\ L \geq 0 \end{cases} \quad (7)$$

where $P_x(L)$ is the cross-correlation at lag day L, N is the time series length, $\bar{\tau}$ is the mean for time series τ, and $\bar{\eta}$ is the mean for time series η. Cross-correlation also ranges from -1 to 1, with 1 denoting perfect correlation and -1 denoting perfect anti-correlation. Again, when cross-correlation falls below 1/*e*, the observed pattern does not persist.

5.1.4 Algorithm Details

The algorithms for calculating both autocorrelation and cross-correlation follow the same general methodology. Since the MODIS is still operational, each algorithm is written such that new data can be easily added to the analysis. First, after inputting all available optical depth data, the daily one degree resolution data are averaged into a two degree grid to remove noise from the dataset. Missing values are then removed

following the deletion method. From here, the 31-day boxcar average for each time series is computed and subtracted from the corresponding optical depth data in the original time series. This step requires optical depth data from one month before and after the period of interest. Here, calculating the 31-day boxcar average for the time period spanning from September 2002 through September 2006 results in a time series from roughly mid-September 2002 through mid-September 2006. The resulting residual time series is now used for the analysis.

The correlation is then calculated at each grid point for the time period in question (here, the time period is northern hemispheric summer and winter). For cross-correlation, the correlation at each grid point is calculated with all points within ±20˚. For the deletion method to hold, a missing data threshold is set to determine if calculations will proceed at each grid point; specifically, locations with missing data accounting for greater than 20% of the time series are omitted from correlation calculations. Correlation is calculated for each year, and is subsequently averaged over the number of years to obtain the mean seasonal correlation at each location.

5.2 Results

5.2.1 Autocorrelation

One day lagged autocorrelation computed at each two degree grid point over the entire earth is shown in Fig. 39 for (a) the northern hemispheric summer and (b) the northern hemispheric winter. The images are scaled as indicated by the color bars at right. Here, regions of dark red correspond to large autocorrelation, and, subsequently,

ice cloud patterns that persist through one day. These regions generally correspond to the regions with low ice cloud frequency of occurrence, as can be observed in the previous Fig. 17 and 18. Multiple periods of consecutive days with no observed ice cloud (i.e., ice cloud optical depth is equal to zero) result in large autocorrelation. Blue regions denote anti-correlation; a cursory analysis reveals that these regions generally correspond to the high frequency regions of Fig. 17 and 18.

5.2.2 Cross-Correlation

Cross-correlation of daily ice cloud optical depth is computed on two degree intervals over the entire earth. However, due to the threshold set on the amount of missing data, the polar regions are filtered from the calculations. At each location, the time series is correlated with the surrounding time series located within ±20 degrees latitude/longitude. For zero lag days, the cross-correlation at each location is equal to one (i.e., zero day lagged autocorrelation); correlation then decreases when moving away from that location. Ice cloud pattern movement is determined from the one day lagged correlations. At one lag day, any movement of the center of the correlation maximum from the location under consideration to another location with the ±20 degree latitude/longitude box indicates movement of the ice cloud pattern.

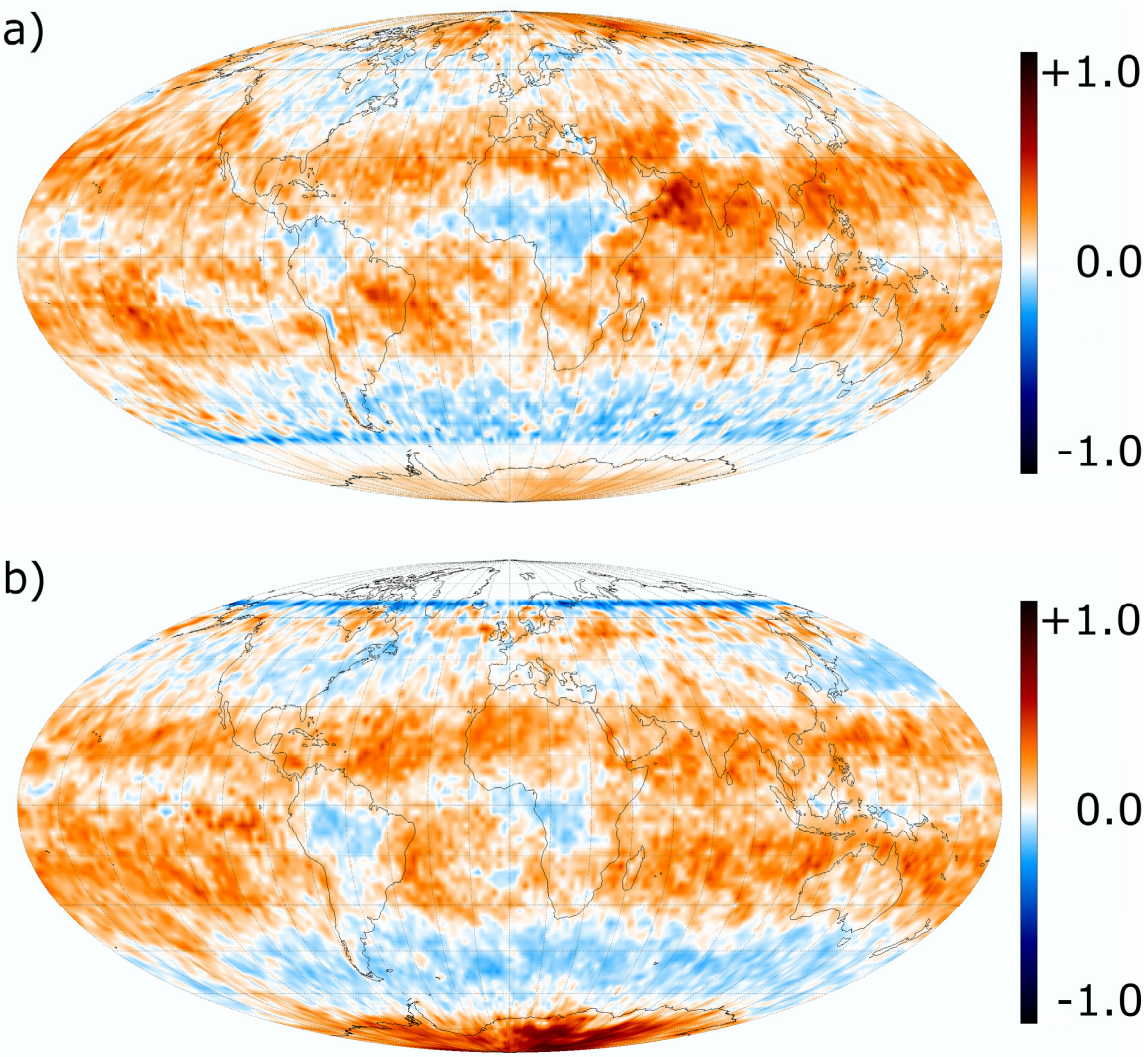

Fig. 39. Autocorrelation calculated at 1 lag day for the northern hemispheric (a) summer and (b) winter.

Figure 40(a) and (b) show the cross-correlation calculated during the northern hemispheric winter for zero day and one day lag, respectively, over a location off the east coast of the United States (29.5N, 75.5W). Note that at the location, the zero day lagged correlation is at a maximum (correlation equals one), and falls off when moving outward. The pattern appears to be well-formed. The one day lagged correlation (b) illustrates the movement of the pattern after one day. Here, it has moved to the northeast, as indicated by the vector, and is now located over Nova Scotia. This shift appears to follow the general movement of the strong low pressure systems and associated fronts that progress across the U.S. during local winter.

The shift in the location of the correlation maximum in Fig. 40, which follows the movements of North American winter frontal systems, demonstrates the capability of this technique in diagnosing how ice clouds move in the atmosphere. Plotting a field of movement vectors over the earth may provide insight into the general mechanisms of formation and dissipation of such clouds. Fig. 41(a) shows the field of movement vectors corresponding to the northern hemispheric summer months. Movement vectors point from the maximum of the zero day lagged cross-correlation to the maximum of the one day lagged cross-correlation. Red vectors denote movements in which the cross-correlation remains statistically significant (i.e., is greater that $1/e$) after one lag day. Fig. 41(b) shows the red vectors from (a), plotted separately for clarity.

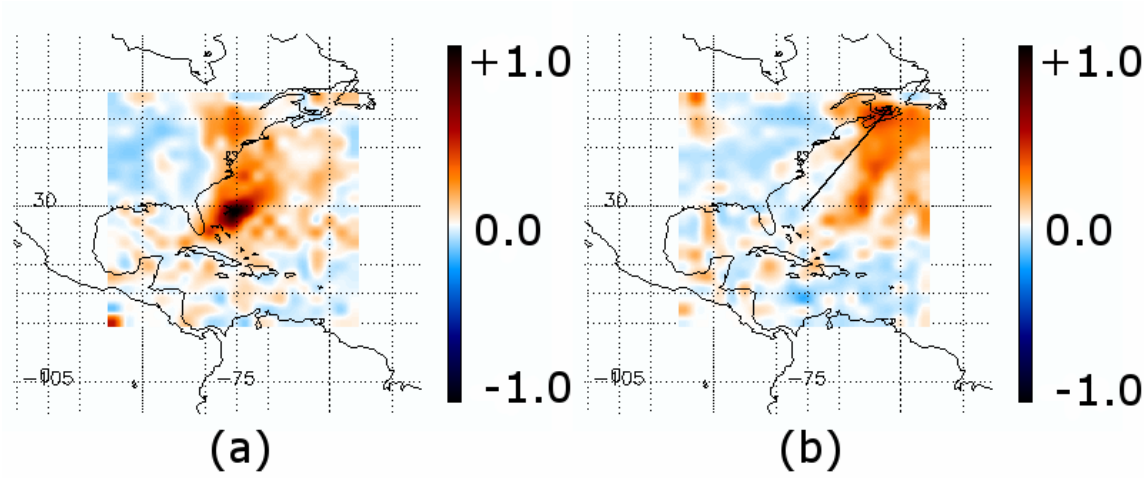

Fig. 40. Cross-correlation of daily ice cloud optical depth calculated during the northern hemispheric winter at a location off the east coast of the Unites States (29.5N, 75.5W). (a) Zero day lagged cross-correlation. (b) One day lagged cross-correlation corresponding to the location in (a). The arrow denotes the movement of the maximum correlation.

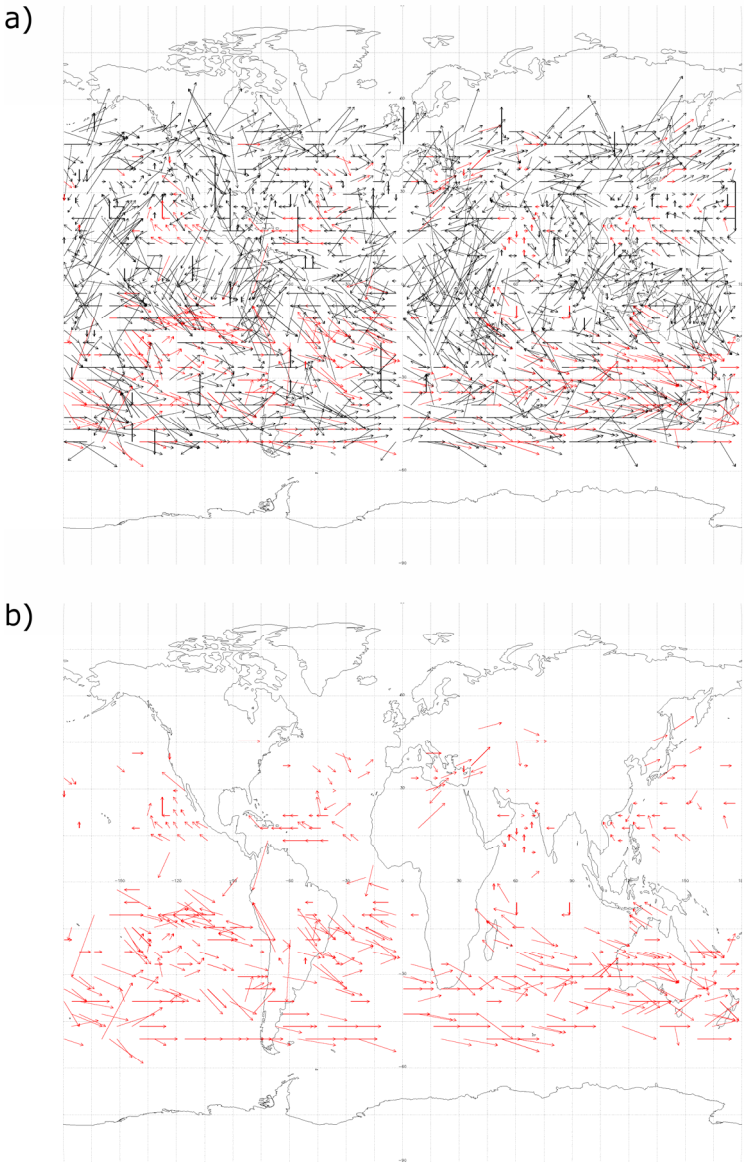

Fig. 41. Sample movement vectors of daily ice cloud optical depth for the northern hemispheric summer months. (a) Vector field illustrating the movement of the zero to one day lagged cross-correlation. Red vectors denote movement in which the one day lagged correlation remains statistically significant (i.e., greater than 1/*e*). (b) The red vectors from (a), plotted separately for clarity.

Fig. 42(a) shows the field of movement vectors corresponding to the northern hemispheric winter months. Again, movement vectors point from the maximum of the zero day lagged cross-correlation to the maximum of the one day lagged cross-correlation. Red vectors denote movements in which the cross-correlation remains statistically significant (i.e., is greater that $1/e$) after one lag day. Fig. 42(b) shows the red vectors from (a), plotted separately for clarity.

At first glance, the movement vector fields in Fig. 41 and 42 appear to be quite random. However, a closer analysis reveals that both exhibit patterns indicating that ice cloud movements may show some sort of general large-scale movement. Fig. 43 shows seasonal 300 mb vector wind means for (a) the northern hemispheric summer months and (b) the northern hemispheric winter months. Vector arrows indicate wind direction, shading indicates the magnitude of the velocity. These plots are taken from the NCEP (National Centers for Environmental Prediction) model re-analysis (Kalnay et al., 1996).

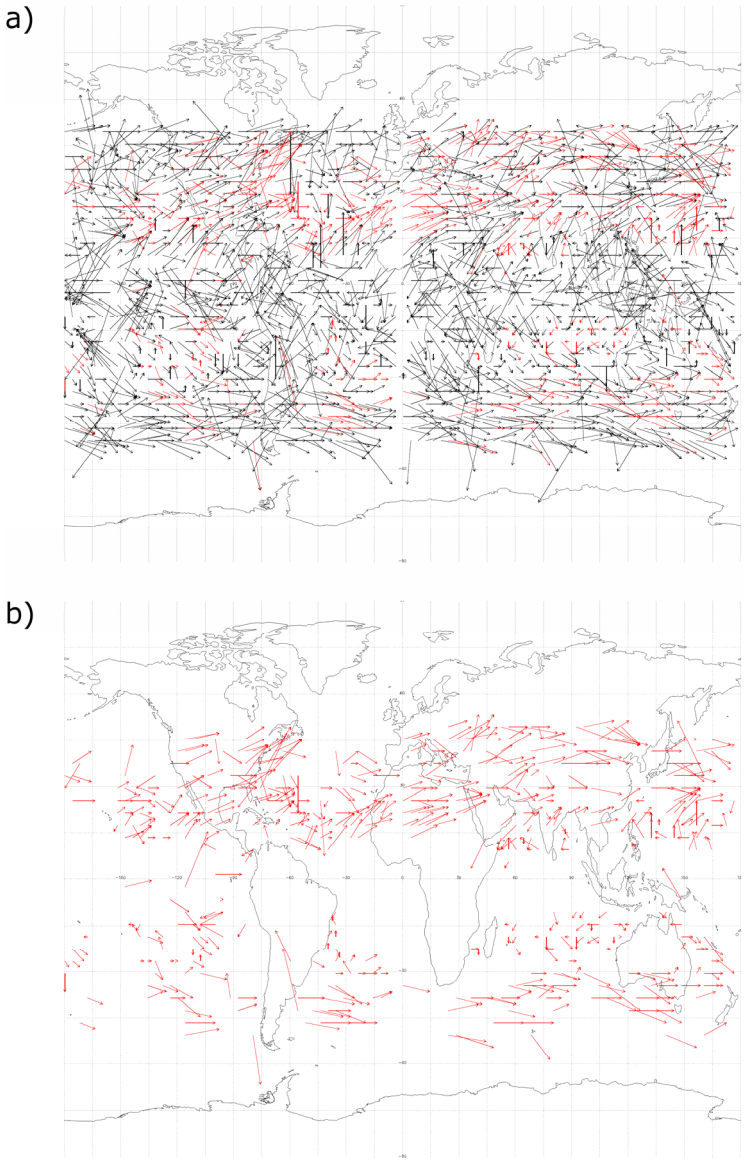

Fig. 42. Sample movement vectors of daily ice cloud optical depth for the northern hemispheric winter months. (a) Vector field illustrating the movement of the zero to one day lagged cross-correlation. Red vectors denote movement in which the one day lagged correlation remains statistically significant (i.e., greater than 1/*e*). (b) The red vectors from (a), plotted separately for clarity.

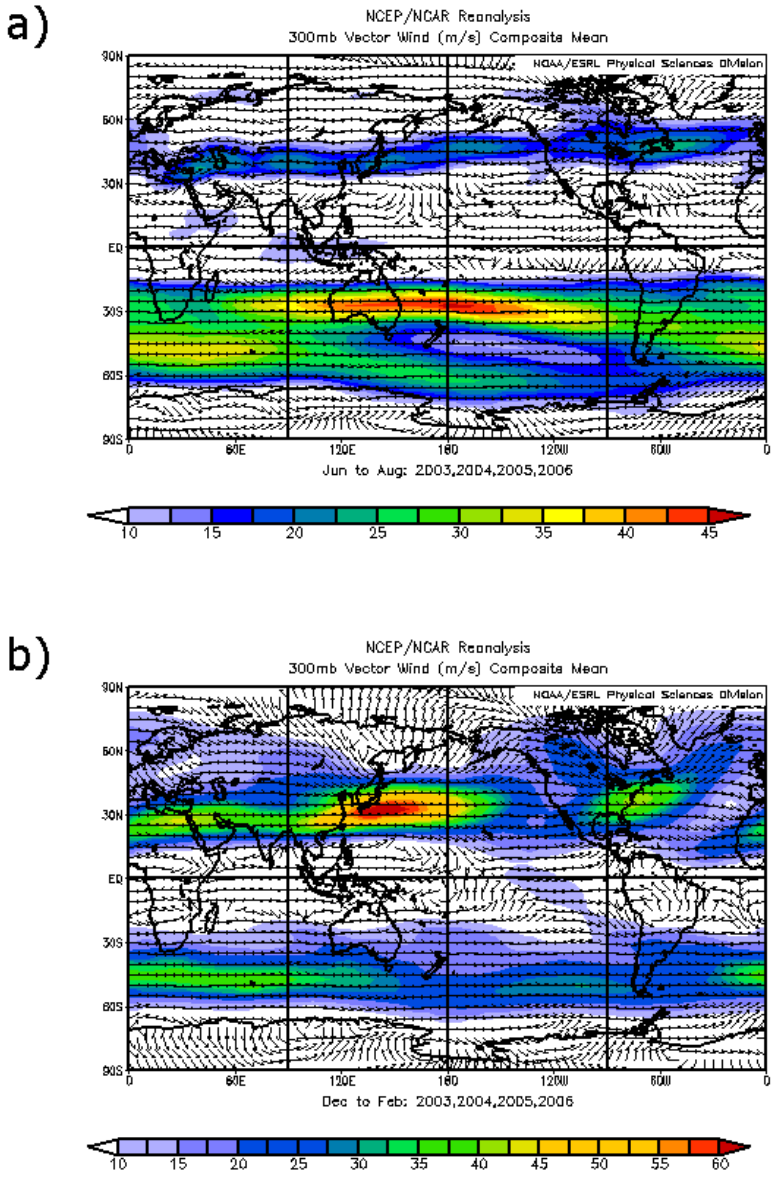

Fig. 43. Seasonal mean NCEP reanalysis 300 mb vector wind for the northern hemispheric summer (a) and winter (b) months. (Image provided by the NOAA/ESRL Physical Sciences Division, Boulder Colorado from their Web site at http://www.cdc.noaa.gov/)

It appears that the regions of statistically significant movement in Fig. 41 and 42 correspond quite well to the jets in Fig. 43. In regions with relatively weak winds (small velocity magnitudes), such as the ITCZ, the movement vectors are randomly oriented. This may signify that, generally speaking, ice clouds within these regions tend to form with the deep convection characteristic of the ITCZ, and dissipate within one day. Further investigation reveals that zero day lagged cross-correlation maximums within these regions are much smaller, when comparing the width of the pattern, than those in Fig. 40(a). This indicates a more localized formation process. An example of these localized maxima is shown in Fig. 44, the zero day lagged cross-correlation for a location over eastern equatorial South America (1.5N, 51.5W). Note the small size of the correlation maximum compared to that in Fig. 40(a). Ice clouds located near the jet regions appear to persist for longer periods of time, and are most likely associated with the storm systems characteristic of the higher latitudes.

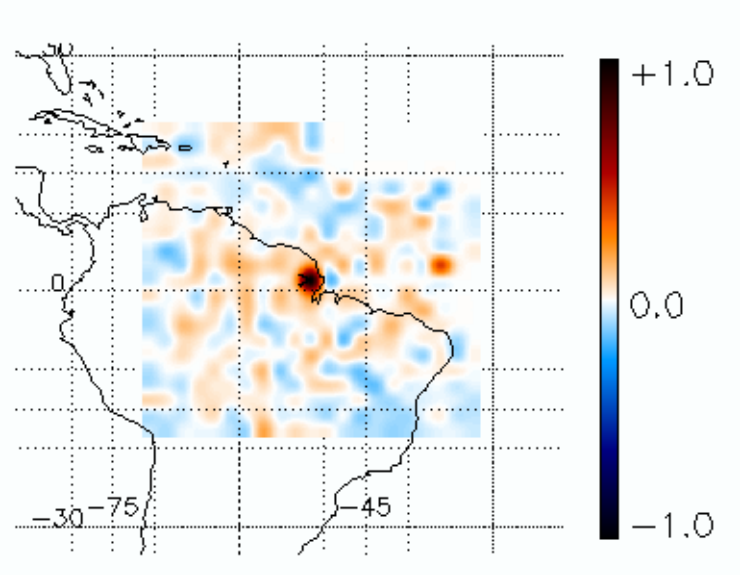

Fig. 44. Zero day lagged cross-correlation of daily ice cloud optical depth over eastern equatorial South America (1.5N, 51.5W).

5.3 Summary

A statistical analysis, following the method of Cahalan et al. (1982), of time series of daily ice cloud optical depth has been undertaken. Daily optical depth is derived from the level-3 MODIS cirrus reflectance parameter using the technique detailed in Section 3. Tools such as autocorrelation and cross-correlation are used to determine the persistence and movement of ice cloud patterns on a global scale. It has been found that the statistical movement of ice clouds in mid-latitudes follows the upper level wind fields, indicating these clouds are most likely associated with the low pressure systems characteristics of these regions. In the tropics, ice cloud movement vectors are randomly oriented and statistically insignificant (one day lagged cross-correlation maxima fall below $1/e$). The localized nature of the zero day lagged cross-correlation maxima in the tropics suggests that these ice clouds are associated with the deep convection characteristic of this region, and the lack of persistence indicates these clouds dissipate relatively quickly (within one day).

6. SUMMARY AND CONCLUSIONS

Ice clouds occur quite frequently, yet so much about these clouds is not understood. In recent years, numerous instruments, investigations, and field campaigns have been developed for and devoted to the study of ice clouds, all with the ultimate goal of gaining a better understanding of the microphysical and optical properties, as well as determining their radiative impact. Perhaps one of the most recognized instruments, not only for ice cloud research but atmospheric research, as well, is the MODIS. Currently, MODIS is flown aboard the NASA EOS satellites Terra and Aqua.

The research presented here aims to support ongoing efforts in the field of ice cloud research by use of observations obtained from both Terra and Aqua MODIS. First, a technique is developed to infer ice cloud optical depth from the cirrus reflectance parameter included in the operational MODIS atmosphere product. This technique is based on a previous method developed by Meyer et al. (2004). The applicability of the algorithm is demonstrated with retrievals from level-2 and -3 MODIS data. The technique is also evaluated against the operational MODIS cloud retrieval product and a method based on airborne ice cloud observations.

From this technique, an archive of daily optical depth retrievals is constructed. Using simple statistics, the general spatial and temporal distributions of global ice clouds are determined. It is found that Aqua MODIS observes more frequent ice clouds and larger optical depths and ice water path than does Terra MODIS. It is also discovered

that there is no trend in the globally averaged ice cloud frequency, optical depth, and ice water path, although shorter-scale seasonal fluctuations are quite evident.

Finally, an analysis of the time series of daily optical depth values is undertaken. Here, statistical tools such as autocorrelation and cross-correlation are used to determine the persistence and movement, respectively, of ice clouds. It is found that ice clouds at high latitudes, which are most likely associated with synoptic scale weather systems, persist long enough to move with the upper level winds. Tropical ice clouds, however, dissipate more rapidly, and are in all likelihood associated with deep convective cells.

REFERENCES

Baran, A. J., P. N. Francis, S. Havemann, and P. Yang, 2001. A study of the absorption and extinction properties of hexagonal ice columns and plates in random and preferred orientation, using exact T-matrix theory and aircraft observations of cirrus. Journal of Quantitative Spectroscopy and Radiative Transfer 70, 505-518.

Baum, B. A., A. J. Heymsfield, P. Yang, and S. T. Bedka, 2005. Bulk scattering properties for the remote sensing of ice clouds. Part I: Microphysical data and models. Journal of Applied Meteorology 44, 1885-1895.

Baum, B. A., P. Yang, A. J. Heymsfield, S. Platnick, M. D. King, Y.-X. Hu, and S. T. Bedka, 2005. Bulk scattering properties for the remote sensing of ice clouds. Part II: Narrowband models. Journal of Applied Meteorology 44, 1896-1911.

Baum, B. A., D. P. Kratz, P. Yang, S.C. Ou, Y. Hu, P. Soulen, and S. C. Tsay, 2000. Remote sensing of cloud properties using MODIS airborne simulator imagery during SUCCESS, 1, Data and Models. Journal of Geophysical Research 105, 11767-11780.

Cahalan, R. F., D. A. Short, and G. R. North, 1982. Cloud Fluctuation Statistics. Monthly Weather Review 110, 26-43.

Chandrasekhar, S., 1950. Radiative Transfer. Dover.

Davis, S. M., Hallar. A.G, Avallone, L.M., and W.E. Engblom, 2007. Measurements of total water content with a tunable diode laser hygrometer: Inlet analysis,

calibration procedure, and ice water content determination. Journal of Atmospheric and Oceanic Technology 24 (3), 463-475.

Dessler, A. E., and P. Yang, 2003. The distribution of tropical thin cirrus clouds inferred from Terra MODIS data. Journal of Climate 16, 1241-1247.

Gao, B.-C., and Y. J. Kaufman, 1995. Selection of the 1.375-μm MODIS channel for remote sensing of cirrus clouds and stratospheric aerosols from space. Journal of Atmospheric Sciences 52, 4231-4237.

Gao, B.-C., K. Meyer, and P. Yang, 2004. A new concept on remote sensing of cirrus optical depth and effective ice particle size using strong water vapor absorption channels near 1.38 and 1.88 μm. IEEE Transactions on Geoscience and Remote Sensing 42, 1891-1899.

Gao, B.-C., P. Yang, W. Han, R.-R. Li, and W. J. Wisombe, 2002. An algorithm using visible and 1.38-μm channels to retrieve cirrus cloud reflectances from aircraft and satellite data. IEEE Transactions on Geoscience and Remote Sensing 40, 1659-1668.

Hallar, A. G., L. M. Avallone, R. L. Herman, B. E. Anderson, and A. J. Heymsfield, 2004. Measurements of ice water content in tropopause region Arctic cirrus during the SAGE III Ozone Loss and Validation Experiment (SOLVE). Journal of Geophysical Research 109, D17203, doi:10.1029/2003JD004348.

Hong, G., P. Yang, B.-C. Gao, B. A. Baum, Y. X. Hu, M. D. King, and S. Platnick. High cloud properties from three years of MODIS Terra and Aqua Data over the Tropics. Journal of Applied Meteorology and Climatology, to be published.

Hu, Y.-X., B. Wielicki, B. Lin, G. Gibson, S.-C. Tsay, K. Stamnes, and T. Wong, 2000. δ-Fit: A fast and accurate treatment of particle scattering phase functions with weighted singular-value decomposition least-squares fitting. Journal of Quantitative Spectroscopy and Radiative Transfer 65, 681-690.

Jensen, E. J., O. B. Toon, L. Pfister, and H. B. Selkirk, 1996. Dehydration of upper troposphere and lower stratosphere by subvisible cirrus clouds near the tropical tropopause. Geophysical Research Letters 23, 825-828.

Kalnay, E. and Coauthors, 1996. The NCEP/NCAR Reanalysis 40-year Project. Bulletin of the American Meteorological Society 77, 437-471.

King, M. D., W. P. Menzel, Y. J. Kaufman, D. Tanré, B. C. Gao, S. Platnick, S. A. Ackerman, L. A. Remer, R. Pincus, and P. A. Hubanks, 2003. Cloud and aerosol properties, precipitable water, and profiles of temperature and humidity from MODIS. IEEE Transactions on Geoscience and Remote Sensing 41, 442-458.

King, M. D., S. –C. Tsay, S. E. Platnick, M. Wang, and K. N. Liou, 1997. Cloud retrieval algorithms for MODIS: Optical thickness, effective particle radius and thermodynamic phase. MODIS Algorithm Theoretical Basis Document, NASA.

Liou, K. N., Y. Takano, and P. Yang, 1999. Light scattering and radiative transfer in ice crystal clouds: applications to climate research. In: M. I. Mishchenko, J. W. Hovenier, L. D. Travis (Eds.), Light scattering by nonspherical particles: theory, measurement, and applications, Academic Press.

Lynch, D. K., K. Sassen, D. O. Starr and G. Stephens (Eds.), 2002. Cirrus. Oxford Univ. Press.

McFarquhar. G. M., 2000. Comments on 'Parameterization of effective sizes of cirrus-cloud particles and its verification against observations' by Zhian Sunand Lawrie Rikus (October B, 1999, 125, 3037-3055). Quarterly Journal of the Royal Meteorological Society 126, 261-266.

Menzel, W. P., D. P. Wylie, K. I. Strabala, 1983. Seasonal and diurnal changes in cirrus clouds as seen in four years of observations with the VAS. Journal of Applied Meteorology 22, 377-384.

Meyer, K., P. Yang, and B.-C. Gao, 2004. Optical thickness of tropical cirrus clouds derived from the MODIS 0.66- and 1.375-μm channels. IEEE Transactions on Geoscience and Remote Sensing 42, 833-841.

Meyer, K., P. Yang, and B.-C. Gao, 2007. Ice cloud optical depth from MODIS cirrus reflectance. IEEE Geoscience and Remote Sensing Letters, doi:10.1109/LGRS.2007.897428.

Meyer, K., P. Yang, and B.-C. Gao, 2007. Tropical Ice Cloud Optical Depth, Ice Water Path, and Frequency Fields Inferred From the MODIS Level-3 Data. Atmospheric Research 85 (2), 171-182.

Minnis, P., P. W. Heck, and D. F. Young, 1993. Inference of cirrus cloud properties from satellite observed visible and infrared radiances. Part II: Verification of theoretical radiative properties. Journal of Atmospheric Sciences 50, 1305-1322.

Pilewskie, P., A. F. H. Goetz, D. A. Beal, R. W. Bergstrom, and P. Mariani, 1998. Observations of the spectral distribution of solar irradiance at the ground during SUCCESS. Geophysical Research Letters 25, 1141-1144.

Platnick, S., M. D. King, S. A. Ackerman, W. P. Menzel, B. A. Baum, J. C. Riedi, and R. A. Frey, 2003. MODIS cloud products: algorithms and examples from Terra. IEEE Transactions on Geoscience and Remote Sensing 41, 459-473.

Rankin, E. D., and J. C. Marsh, 1985. Effects of missing data on the statistical analysis of clinical time series. Social Work Research Abstracts 21, 13-16.

Stamnes, K., S.-C. Tsay, W. Wiscombe, and K. Jayaweera, 1988. Numerically stable algorithm for discrete-ordinate-method radiative transfer in multiple scattering and emitting layered media. Applied Optics 27, 2505-2509.

Starr, D. O., 1987. A Cirrus-Cloud Experiment: Intensive Field Observations Planned for Fire. Bulletin of the American Meteorological Society 68, 2, 119-124.

Stephens, G. L., S. -C. Tsay, P. W. Stackhouse, and P. J. Flatau, 1990. The relevance of the microphysical and radiative properties of cirrus clouds to climate and climatic feedback. Journal of Atmospheric Sciences 47, 1742–1753.

Tsay, S.-C., P. M. Gabriel, M. D. King, and G. L. Stephens, 1996. Spectral reflectance and atmospheric energetics in cirrus-like clouds. Part II: Applications of a Fourier-Riccati approach to radiative transfer. Journal of Atmospheric Sciences 53, 3450-3467.

Wang, P.-H., M.P. McCormick, L. R. Poole, W. P. Chu, G. K. Yue, G. S. Kent, and K. M. Skeens, 1994. Tropical high cloud characteristics derived from SAGE II extinction measurements. Atmospheric Research 34 (1-4), 53-83.

Wendisch, M., P. Pilewskie, J. Pommier, S. Howard, P. Yang, A. J. Heymsfield, C. G. Schmitt, D. Baumgardner, and B. Mayer, 2005. Impact of cirrus crystal shape on

solar spectral irradiance: A case study for subtropical cirrus. Journal of Geophysical Research 110.

Wiscombe. W., 1977. The delta–*M* method: Rapid yet accurate radiative flux calculations for strongly asymmetric phase functions. Journal of Atmospheric Sciences 34, 1408-1422.

Wylie, D. P., D. L. Jackson, W. P. Menzel, and J. J. Bates, 2005. Trends in global cover in 22 years of HIRS observations. Journal of Climate 18, 3021-3031.

Wylie, D. P., and W. P. Menzel, 1999. Eight years of high cloud statistics using HIRS," Journal of Climate 12, 170-184.

Wylie, D. P., W. P. Menzel, H. M. Woolf, and K. I. Strabala, 1994. Four years of global cirrus cloud statistics using HIRS. Journal of Climate 7, 1972-1986.

Yang, P., K. N. Liou, K. Wyser, and D. Mitchell, 2000. Parameterization of the scattering and absorption properties of individual ice crystals. Journal of Geophysical Research 105, 4699-4718.

Zhang, Y., A. Macke, and F. Albers, 1999. Effect of crystal size spectrum and crystal shape on stratiform cirrus radiative forcing. Atmospheric Research 52 (1-4), 59-75.

VITA

Name: Kerry Glynne Meyer

Address: 3150 TAMU, College Station, TX 77843-3150

Email Address: kmeyer@ariel.met.tamu.edu

Education: B.S., Meteorology, Texas A&M University, 2001
M.S., Atmospheric Sciences, Texas A&M University, 2004

Publications:

Meyer, K., P. Yang, and B,-C. Gao, 2007. Ice cloud optical depth from MODIS cirrus reflectance. IEEE Geoscience and Remote Sensing Letters doi:10.1109/LGRS.2007.897428.

Meyer, K., P. Yang, and B.-C. Gao, 2007. Tropical ice cloud optical depth, ice water path, and frequency fields inferred from the MODIS level-3 data. Atmospheric Research doi:10.1016/j.atmosres.2006.09.009.

Gao, B.-C., K. Meyer, and P. Yang, 2004. A new concept on remote sensing of cirrus optical depth and effective ice particle size using strong water vapor absorption channels near 1.38 and 1.88 mm. IEEE Transactions on Geoscience and Remote Sensing 42, 1891-1899.

Meyer, K., P. Yang, and B.-C. Gao, 2004. Optical thickness of tropical cirrus clouds derived from the MODIS 0.66- and 1.375-mm channels. IEEE Transactions on Geoscience and Remote Sensing 42, 833-841.